

Theoretical model of swirling thick film flow inside converging nozzles of various geometries

Boo-Hyoung Bang^a, Yong-Il Kim^b, Chan-Sol Ahn^{b,c}, Seokgyu Jeong^d, Youngbin Yoon^d,
Seongpil An^{e,*}, Sam S. Yoon^{b,*}, Alexander L. Yarin^{f,*}

^a Department of Energy Mechanical Engineering, Gyeonggi University of Science and Technology, 269, Gyeonggilwagidae-ro, Siheung-si 15073, Republic of Korea

^b School of Mechanical Engineering, Korea University, Seoul 136-713, Republic of Korea

^c Fire Research Center, Korea Institute of Civil Engineering and Building Technology, 283, Goyang-daero, Ilsanseo-gu, 10223 Goyang-si, Republic of Korea

^d Department of Mechanical and Aerospace Engineering, Seoul National University, Seoul 08826, Republic of Korea

^e SKKU Advanced Institute of Nanotechnology (SAINT) Department of Nano Engineering Sungkyunkwan University (SKKU), Suwon 16419, Republic of Korea

^f Department of Mechanical and Industrial Engineering, University of Illinois at Chicago, 842 W. Taylor St., Chicago IL 60607-7022, USA

ARTICLE INFO

Keywords:

Swirling jet
Thick film
Nozzle geometry
Swirling strength
The Reynolds number

ABSTRACT

Pressure-swirl jets are of paramount importance in such applications as liquid rockets, gas turbines, and internal combustion engines. Although the external spray has been extensively studied, the internal nozzle flow, which determines the external spray characteristics outside the nozzle, is relatively underexplored. Experimental studies of the internal nozzle flow are available, whereas theoretical approaches are less common, especially for strong swirl flows in which the boundary layer effect at the nozzle walls is significant. Herein, we explore a strongly swirling film flow, where viscous effects become dominant in the entire film and the boundary-layer approximation fails. The parabolized Navier-Stokes equations are solved by using the integral von Karman-Pohlhausen method, and the viscous liquid film flow over the entire nozzle wall is predicted including the central free surface configuration, the film characteristics such as its thickness, velocity components, and the spray cone angle, at the nozzle exit. The theoretical predictions are compared to the experimental data, and the dependence of the spray-cone angle on mass flow rate is experimentally validated. The theoretical parametric studies include the effect of the internal nozzle geometry, initial film thickness, the mass flow rate, and the effect of the swirling strength.

1. Introduction

Pressure-swirl atomizers are widely used in industrial applications, such as liquid rocket engines, gas turbine engines, and internal combustion engines, because of their reliability, high throughput, and good atomization performance [1–4]. The liquid is injected into tangential ports, thereby inducing centrifugal force. As a result, an air core is formed at the center and the bulky annular liquid film rotates inside an upper chamber of the atomizer. This rotating liquid travels downstream and undergoes laminarization through a converging nozzle that is connected to a straight orifice, where a thin liquid film is moving over the inner wall of the orifice.

There are numerous experimental [5–9] and numerical [2,8,10–13] studies on pressure-swirl atomizers. Theoretical studies are of particular interest as they allow prediction of the initial conditions at the nozzle exit for the swirling liquid sheet, which eventually breaks up into

droplets.

G.I. Taylor theorized this swirling liquid as an inviscid flow and analytically predicted the air core radius and the discharge coefficient [14]. A similar study by Giffen and Murazew and Abramovich produced exactly the same results as those of Taylor [15,16], as reported by Chinn [17]. Taylor provided a viscous model later, accounting for the fact that the swirling film is affected by the viscous boundary layer, which slows down the swirling motion closer to the walls [18]. As usual in the boundary layer theory, Taylor separated the entire swirling film in the nozzle into two separate zones: the outer flow, i.e., the liquid closer to the centerline treated as an inviscid (potential) core, and the near-wall viscous boundary layer, with matching in-between [18]. Taylor assumed that the inviscid core experienced no axial motion, while the viscous boundary layer streamed down in the axial direction. Binnie and Harris provided a more comprehensive analysis that considered the axial motion in the inviscid (potential) core zone [19].

* Corresponding authors.

E-mail addresses: esan@skku.edu (S. An), skyoona@korea.ac.kr (S.S. Yoon), ayarin@uic.edu (A.L. Yarin).

<https://doi.org/10.1016/j.fuel.2020.118215>

Received 20 March 2020; Received in revised form 12 May 2020; Accepted 25 May 2020

0016-2361/© 2020 Elsevier Ltd. All rights reserved.

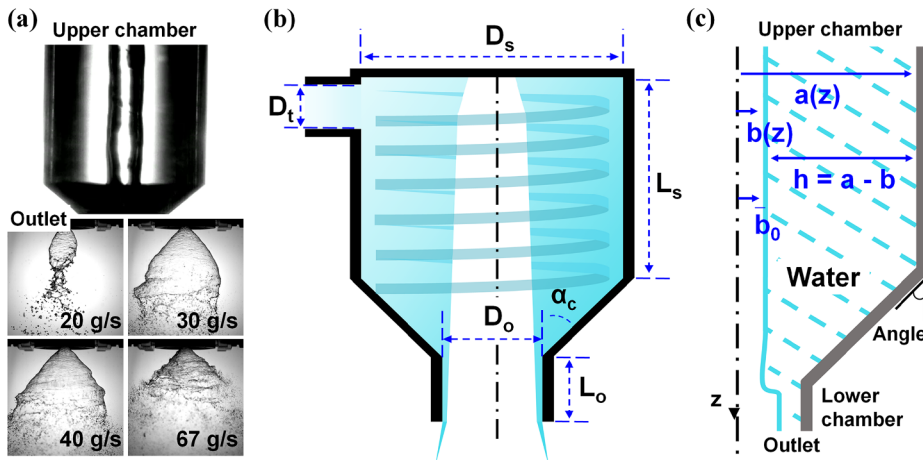


Fig. 1. (a) Upstream swirling air column inside the nozzle and external atomized liquid sheet at various flow rates. (b) Schematic depicting nozzle configuration. (c) Parameters characterizing the swirling film: $a(z)$ is the nozzle profile, with z being the axial coordinate, $b(z)$ is the free surface radius, $h(z) = a - b$ is the film thickness, and b_0 is the initial free surface radius rendered dimensionless by the entrance nozzle radius.

Binnie and Harris reproduced Taylor’s solution in the particular case of excluded axial motion in the core [19]. When both swirling and axial motions were considered, the film was thinner than that predicted by the Taylor solution. However, the treatments of Taylor and Binnie and Harris both fail when the swirl is strong ($\Omega^2/2a_c^2 \geq P/\rho$, where $\Omega = \Gamma/2\pi$ and Γ is the swirl circulation, a_c is the nozzle exit radius, ρ is the liquid density, and P is the pressure at the nozzle entrance) [18,19]. When $\Omega^2/2a_c^2 = P/\rho$, the boundary-layer-based theory predicts that the entire cross-section becomes a funnel, and the axial velocity of the film becomes zero, i.e., the entire pressurization is converted into the swirl, and the longitudinal flow ceases. At $\Omega^2/2a_c^2 > P/\rho$ there is no physical solution at all. The failure of the boundary-layer-based theory shows that in the case of the strong swirl viscous forces should be accounted for in the entire film using the Navier-Stokes equations, which has not been attempted so far.

Wimmer and Brenn separated the entire rotating liquid into three zones: the first zone is the viscous region in contact with the chamber wall [20]. The third zone is the relatively thin region near the centerline. The second zone is the region between the first and third zones. In the first and second zones, the axial motion is assumed to be zero and the zones are treated as a 2D flow in the radial (r) and tangential (θ) directions, while the third zone is treated as a fully 3D flow. Notably, the swirl nozzle of Wimmer and Brenn differs from the classical geometry of a swirl nozzle in that the converging nozzle section is omitted [20]. Amini [21] and Dumouchel et al. [22] also used the boundary-layer based approach as Taylor and Binnie and Harris, while considering the classical swirl nozzle shape with a converging section. The effect of the Reynolds number and nozzle geometry on the film thickness, spray angle, and discharge coefficient was studied.

Recently, Bang et al. [23] studied very thin films in nozzles with smoothly-varying profile. They used the von Karman-Pohlhausen method, which reduces the full 3D Navier-Stokes equations to quasi-one-dimensional equations in the lubrication approximation. This is essentially a long-wave approximation, which precludes consideration of situations in which the film thickness is comparable to the nozzle radius, and the nozzle profile changes abruptly. In the swirl atomizers of interest here, the film thickness can be comparable to the orifice radius, and the nozzle profile can change abruptly, which makes the approach of [23] inapplicable.

For this reason, we use here the fully 3D parabolized Navier-Stokes equations, which are solved using the integral von Karman-Pohlhausen method. Accordingly, the viscous liquid film profile over the entire nozzle is predicted without separating the film into various zones. The liquid film thickness is predicted for any required nozzle geometry, mass flowrate, and swirl strength. The axial and radial velocities of the exiting film are predicted, and thus the liquid sheet cone angle is also estimated. This fully 3D approach is meaningful in that the entire “thick” film is treated as a 3D fully viscous flow.

2. Experimental

Fig. 1a presents images of the upstream internal flow and downstream external spray from experiments. The internal flow is the rotating liquid column with an air core around the centerline (a funnel), induced by the centrifugal force. The external flow is a diverging cone spray, which varies with the flow rate. The measured cone spray angles are to be compared with the theoretical predictions. Fig. 1b illustrates the nozzle profile used in the experiments and the corresponding theory. Fig. 1c shows the parameters used to describe the internal flow liquid film, wherein $a(z)$ is the nozzle outer radius distribution in the axial z -direction, $b(z)$ is the funnel free surface radius, $h(z) = a - b$ is the film thickness, and b_0 is the initial free surface radius rendered dimensionless by the entrance nozzle radius.

The experimental details are described in depth by Chung et al. [24]. The important outlines are briefly summarized herein. The experimental apparatus is shown in Fig. 2. Water was used as the experimental fluid. As shown in Fig. 2, water was injected by pressurized air using a compressor. The required flow rate was controlled by a regulator (accuracy: ± 0.02 atm) and measured by a flow meter (Hoffer Flow Control, HO1/2X1/4A-0.35-3.5-BP-1MX-MS-X, uncertainty: $\pm 0.49\%$) installed in the feed line. A high-speed camera (Lavision, Highspeed Star8) and continuous light source (Photron, HVC-SL) were used to obtain the spray backlit image. The images were acquired at 50 fps with a pixel resolution of 1024×1024 . A closed-type swirl injector was used in the experiment. The geometry of the swirl injector was as follows: the swirl chamber length (L_s) was 30 mm, the swirl chamber diameter (D_s) was 20 mm, the orifice diameter (D_o) was 6 mm (i.e., $D_o/D_s = 0.3$), the number of tangential inlet ports (N_t) was 3, and the

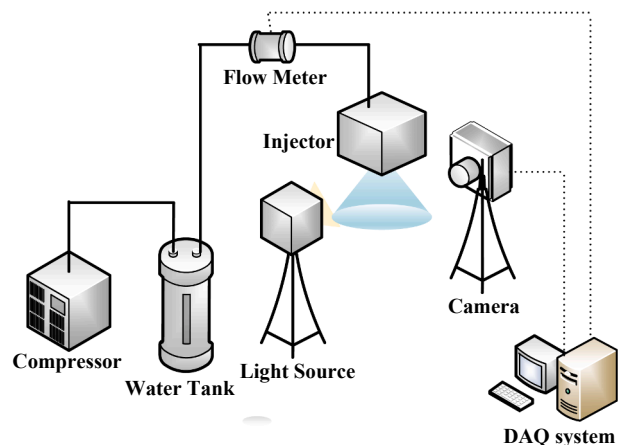


Fig. 2. Experimental apparatus.

tangential inlet port diameter (D_i) was 1.4 mm. The convergence angle (α_c) of the nozzle convergent section was 45°.

In general, swirl injectors provide high atomization quality with a simple geometry and small volume. This is possible because of the swirling effect. Notably, the closed-type swirl injector offers the advantage of achieving a larger spray-cone angle and higher spray performance than the open-type swirl injector because the closed-type swirl injector can provide higher angular velocity at the orifice exit due to the acceleration through the converging section. Thus, herein, the closed-type swirl injector is in focus. When designing an injector, the flow rate and spray angle are important because in the applications these parameters influence the combustion region and combustion chamber size. Therefore, the spray angle is chosen as the main parameter for analysis. Herein, the average spray angle from 100 images was used to achieve statistically sound results.

3. Theoretical

3.1. Limitations of the inviscid and boundary-layer theory in the case of strong swirl

First, summarize the main findings of the inviscid potential theory of swirling liquid film flow over the inner nozzle wall [19]:

- (i) The azimuthal (swirling) velocity component is taken in the form of a potential vortex, as $v_\theta = \Omega/r$, where Ω is a given constant (related to the circulation Γ as $\Omega = \Gamma/2\pi$), which is determined by the inflow geometry. This means that the no-slip condition at the nozzle wall $r = a(z)$ does not hold. Here and hereinafter the cylindrical coordinates are used, with r being the radial coordinate reckoned from the axisymmetric nozzle axis, θ being the angular (azimuthal) coordinate in the nozzle cross-section, and z being the axial coordinate.
- (ii) The radial velocity component v_r is assumed to be zero, i.e., $v_r \approx 0$.
- (iii) The axial velocity component v_z is assumed to be constant in the film cross-section, i.e. the no-slip condition does not hold at the nozzle wall $r = a(z)$.

Because the flow is assumed to be inviscid, the Bernoulli equation globally holds. Using the assumptions (i)-(iii), it takes the form

$$\frac{p}{\rho} = \frac{1}{2} \left(\frac{\Omega^2}{b^2} - \frac{\Omega^2}{r^2} \right) \quad (1)$$

where $r = b(z)$ denotes the free surface of the film. Note that in Eq. (1) the pressure in the funnel $r \leq b$, p_b at $r = b$ is taken to be zero, because in any case it can be subtracted from all pressures. It should be emphasized that the free surface $b(z)$ is to be found.

In addition, the volumetric flow rate Q (which is not given if pressure P in a pressurized vessel is considered to be given, or vice versa) is expressed as

$$Q = \pi(a^2 - b^2)v_z \quad (2)$$

Note that Q is a constant along the film, whereas $a = a(z)$, $b = b(z)$ and $v_z = v_z(z)$ all vary along the film. It should be emphasized that the nozzle profile $a = a(z)$ is a given function.

The analysis based on Eqs. (1) and (2) allows one to find the radius of the free surface of the film $b_e = b(z_e)$ at the exit cross-section $a_e = a(z_e)$, where z_e is the nozzle length ($z = 0$ corresponds to the nozzle entrance), as well as the volumetric flow rate, in the following form [19]

$$\frac{b_e^2}{a_e^2} = \frac{\rho\Omega^2}{8Pa_e^2} \left[1 + \sqrt{1 + \frac{16Pa_e^2}{\rho\Omega^2}} \right], \quad Q = \Omega a_e \frac{\pi}{\sqrt{2}} \frac{(1 - b_e^2/a_e^2)^{3/2}}{b_e^2/a_e^2} \quad (3)$$

Then, the longitudinal velocity in the film can be also found as one of the solutions of the corresponding cubic equation. The velocity

distribution $v_z(z)$ found from such an equation can be used as the outer solution required for matching with the viscous (inner) solution inside the boundary layer near the nozzle wall, as it is done by Taylor and Binnie & Harris [18,19].

However, for a strong swirl, such that

$$\frac{\Omega^2}{2a_e^2} = \frac{P}{\rho} \quad (4)$$

the first Eq. (3) yields $b_e = a_e$, which means that the film ceases! Accordingly, the exit longitudinal velocity $v_{ze} = 0$, if Eq. (4) holds, i.e. the entire pressurization is spent for swirl, and the longitudinal flow ceases! Therefore, the inviscid outer flow described above, and the corresponding boundary layer theory describing the matched inner solution can be found only for the intermediate swirl range, such that

$$0 < \frac{\Omega^2}{2a_e^2} < \frac{P}{\rho} \quad (5)$$

It should be emphasized that the outer solution based on the inviscid theory completely fails in the cases of the strong swirl, such that

$$\frac{\Omega^2}{2a_e^2} \geq \frac{P}{\rho} \quad (6)$$

and thus no boundary-layer solution (and the boundary layer itself) exists. Therefore, in the cases of the strong swirl, the entire film should be treated as viscous, and the description should be based on the Navier-Stokes equations.

3.2. Estimates of the relevant physical parameters

The nozzle of interest in the present work is shown in Fig. 1, with the corresponding notations and geometrical parameters listed in Table 1. The mass flow rate $\dot{M} = 57.3$ g/s related to the injection absolute pressure $P_{inj} = 4$ bar in a pressured vessel. Taking the atmospheric pressure as zero (the free surface pressure, $p_b = 0$), the gage pressure of the vessel is $P = 3$ bar. The liquid density $\rho = 1$ g/cm³. Then, the initial angular velocity can be estimated as $v_{\theta,init} = \dot{M}/(\rho\pi D_i^2/4) = 37.22$ m/s. On the other hand, according to the inviscid theory discussed in Section 3.1, the initial circulation-related

Table 1
Parametric studies.

Case No.	α_c [°]	D_0 / D_s	b_0	\dot{M} [g/s]	Re	β [°]
1A	15	0.3	0.193	57.3	456	52.95
1B	30	0.3	0.193	57.3	456	53.01
1C	45	0.3	0.193	57.3	456	52.87
1D	60	0.3	0.193	57.3	456	53.09
2A	45	0.3	0.193	57.3	456	52.87
2A-a	45	0.32	0.193	57.3	456	82.08
2A-b	45	0.34	0.193	57.3	456	84.71
2A-c	45	0.36	0.193	57.3	456	85.96
2A-d	45	0.38	0.193	57.3	456	86.72
2B	45	0.4	0.193	57.3	456	87.25
2C	45	0.5	0.193	57.3	456	88.55
2D	45	0.6	0.193	57.3	456	89.08
2E	45	0.7	0.193	57.3	456	89.36
3A	45	0.3	0.193	57.3	456	52.87
3B	45	0.3	0.18	57.3	456	81.82
3C	45	0.3	0.17	57.3	456	83.67
3D	45	0.3	0.16	57.3	456	84.61
3E	45	0.3	0.15	57.3	456	85.20
4A	45	0.3	0.193	12	95	44.40
4B	45	0.3	0.193	20	159	50.26
4C	45	0.3	0.193	35	279	52.1
4D	45	0.3	0.193	57.3	456	52.87
4E	45	0.3	0.193	100	796	53.34
4F	45	0.3	0.193	200	1592	53.64
4G	45	0.3	0.193	400	3183	53.78
4H	45	0.3	0.193	1000	7958	53.87

parameter Ω_{init} can be estimated from the equality $v_{\theta,init} = \Omega_{init}/(D_s/2)$, which yields $\Omega_{init} = 0.37 \text{ m}^2/\text{s}$. In the present case, $a_e = D_0/2 = 0.003 \text{ m}$ (cf. Fig. 1). Therefore $\Omega_{init}^2/(2a_e^2) = 7700 \text{ m}^2/\text{s}^2$. On the other hand, $P/\rho = 300 \text{ m}^2/\text{s}^2$. Therefore, the inequality Eq. (6) holds, and the inviscid theory is inapplicable, as well as no boundary-layer-type solution, and the boundary layer itself, exist. This is the case of the strong swirl, and the Navier-Stokes equations should be invoked.

3.3. Solution based on the Navier-Stokes equations

The full system of the Navier-Stokes equations written in the cylindrical coordinates can be found in Ref. [25]. These include the projections of the momentum balance equation onto the radial, azimuthal and axial directions, and the continuity equation. These four scalar equations fully determine the four unknown functions: the velocity components $v_r(r,z)$, $v_\theta(r,z)$, $v_z(r,z)$, and pressure $p(r,z)$.

The system of the Navier-Stokes equations is elliptical. In the pipe and nozzle flows the effect of the terms related to the second derivative in z can be typically neglected, and the following system of the parabolized Navier-Stokes equations [26] arises

$$v_r \frac{\partial v_r}{\partial r} + v_z \frac{\partial v_r}{\partial z} - \frac{v_\theta^2}{r} = -\frac{1}{\rho} \frac{\partial p}{\partial r} + \nu \left[\frac{1}{r} \frac{\partial}{\partial r} \left(r \frac{\partial v_r}{\partial r} \right) - \frac{v_r}{r^2} \right] \quad (7)$$

$$v_r \frac{\partial v_\theta}{\partial r} + v_z \frac{\partial v_\theta}{\partial z} + \frac{v_r v_\theta}{r} = \nu \left[\frac{1}{r} \frac{\partial}{\partial r} \left(r \frac{\partial v_\theta}{\partial r} \right) - \frac{v_\theta}{r^2} \right] \quad (8)$$

$$v_r \frac{\partial v_z}{\partial r} + v_z \frac{\partial v_z}{\partial z} = -\frac{1}{\rho} \frac{\partial p}{\partial z} + \nu \frac{1}{r} \frac{\partial}{\partial r} \left(r \frac{\partial v_z}{\partial r} \right) \quad (9)$$

$$\frac{\partial}{\partial r} (rv_r) + \frac{\partial}{\partial z} (rv_z) = 0 \quad (10)$$

where ν is the kinematic viscosity of the liquid.

The parabolic equations are significantly simpler to solve, even though there might be inaccuracies in the nozzle sections where the second derivative in z is large because of the abrupt geometry change.

It should be emphasized that following the seminal work of Taylor [18], the flow is approximately treated as laminar. This is corroborated by the fact that the seemingly perturbed interface of the air core and the liquid seen in Fig. 1a is mostly an optical artifact, which stems from the observation of the interface through a curved surface amplifying and distorting minor details in the glimpses like that.

In the case of the strong swirl, the main deficiency of the inviscid theory stems from its disregard of the no-slip condition at the nozzle wall. This points at the right-hand side of Eq. (8) as the dominant factor, whereas the inertial terms of that equation can be neglected. Then, Eq. (8) is reduced to the following equation

$$\frac{1}{r} \frac{\partial}{\partial r} \left(r \frac{\partial v_\theta}{\partial r} \right) - \frac{v_\theta}{r^2} = 0 \quad (11)$$

Its solution, which satisfies the no-slip condition $v_\theta = 0$ at $r = a$, and approaches the potential vortex of Refs. [18,19] far from the wall, reads

$$v_\theta = \frac{\Omega_0}{r} \left(1 - \frac{r^2}{a^2} \right) \quad (12)$$

This solution corrects the inviscid potential vortex of Ref. [18,19] discussed in Section 3.1. The constant Ω_0 in Eq. (12) can be evaluated as

$$\Omega_0 \approx \frac{v_{\theta,init} b_0}{(1 - b_0^2/a_0^2)} \quad (13)$$

where $v_{\theta,init}$ is established in Section 3.2, and b_0 and a_0 are the radii of the free surface of the film and the inner nozzle wall at the entrance. Note that $a_0 = D_s/2$.

In the case of the strong swirl, the dominant effect in the radial direction is the centrifugal force, which determines pressure

distribution in the radial direction, i.e., Eq. (7) reduced to

$$\frac{\partial p}{\partial r} = \frac{\rho v_\theta^2}{r} \quad (14)$$

Using Eq. (12), the integration of Eq. (14) yields the pressure in the following form

$$p = \rho \Omega_0^2 \left(\frac{1}{2b^2} - \frac{1}{2r^2} - \frac{2}{a^2} \ln \frac{r}{b} + \frac{r^2}{2a^4} - \frac{b^2}{2a^4} \right) \quad (15)$$

Note that at $r = b$, $p = p_b = 0$, as explained in Sections 3.1 and 3.2.

Accordingly, differentiating Eq. (15) by z , one obtains

$$\frac{1}{\rho} \frac{\partial p}{\partial z} = \Omega_0^2 \left(-\frac{1}{b^3} \frac{db}{dz} + \frac{4}{a^3} \frac{da}{dz} \ln \frac{r}{b} + \frac{2}{a^2 b} \frac{db}{dz} - \frac{2r^2}{a^5} \frac{da}{dz} - \frac{b}{a^4} \frac{db}{dz} + \frac{2b^2}{a^5} \frac{da}{dz} \right) \quad (16)$$

It should be emphasized that at the free surface of the film, the following kinematic condition holds

$$\frac{db}{dz} = \frac{v_r}{v_z} \Big|_{r=b} \quad (17)$$

3.4. Solution by the von Karman-Pohlhausen method

The integral von Karman-Pohlhausen method is a powerful approximate method which can be effectively used to describe the longitudinal motion in the film governed by Eqs. (9), (10), (16) and (17). It has already been used to solve different parabolic problems in cylindrical coordinates, for example, in [19,27,28].

Integrating Eq. (10) in the film cross-section by r from b to a , one obtains the integral volume (and thus, mass) balance in the form

$$-rv_r|_{r=b} + \int_b^a \frac{\partial rv_z}{\partial z} dr = 0 \quad (18)$$

It should be emphasized that in the integration, the no-slip condition $v_r = 0$ at $r = a$ has been accounted for. This condition is also accounted for, when one differentiates the integral depending on parameter z using the standard calculus formula

$$\frac{d}{dz} \int_{b(z)}^{a(z)} rv_z dr = -\frac{db}{dz} rv_z|_{r=b} + \int_b^a \frac{\partial rv_z}{\partial z} dr \quad (19)$$

Using the kinematic condition (17), one finds from Eq. (19) that

$$\int_b^a \frac{\partial rv_z}{\partial z} dr = \frac{d}{dz} \int_b^a rv_z dr + rv_r|_{r=b} \quad (20)$$

Substituting Eq. (20) into Eq. (18), one finds that

$$\frac{d}{dz} \int_b^a rv_z dr = 0 \quad (21)$$

and thus, the integration yields the volume (and thus, the mass) balance in the film in the following form

$$\int_b^a rv_z dr = \frac{Q}{2\pi} \quad (22)$$

where Q is the volumetric flux. Here, the volumetric flux Q is considered to be given, and in principle, can be related to the supply pressure P by considering in detail the flow in the supply system leading to the nozzle.

Using Eq. (10), transform the longitudinal momentum balance Eq. (9) to the following divergent form

$$\frac{\partial rv_r v_z}{\partial r} + \frac{\partial rv_z^2}{\partial z} = -\frac{1}{\rho} r \frac{\partial p}{\partial z} + \nu \frac{\partial}{\partial r} \left(r \frac{\partial v_z}{\partial r} \right) \quad (23)$$

Then, integrating in r in the film cross-section, similarly to the

continuity equation, one obtains

$$-rv_r v_z|_{r=b} + \int_b^a \frac{\partial rv_z^2}{\partial z} dr = -\frac{1}{\rho} \int_b^a r \frac{\partial p}{\partial z} dr + \nu r \frac{\partial v_z}{\partial r} \Big|_{r=a} \tag{24}$$

where in addition to the no-slip condition at the nozzle wall, account is taken of the fact that the absence of the shear forces at the film surface means that $\partial v_z / \partial r|_{r=b} \approx 0$.

Then, similarly to Eq. (20), one obtains

$$\int_b^a \frac{\partial rv_z^2}{\partial z} dr = \frac{d}{dz} \int_b^a rv_z^2 dr + rv_r v_z|_{r=b} \tag{25}$$

and Eq. (24) is transformed to the following integral form

$$\frac{d}{dz} \int_b^a rv_z^2 dr = -\frac{1}{\rho} \int_b^a r \frac{\partial p}{\partial z} dr + \nu a \frac{\partial v_z}{\partial r} \Big|_{r=a} \tag{26}$$

Eqs. (22) and (26) form the system of equations which determine the longitudinal velocity $v_z(r,z)$ and the free surface of the film $b(z)$. Notably, they are fully autonomous from the radial velocity component $v_r(r,z)$. The latter can be, in principle, found from the residual of Eq. (7)

$$v_r \frac{\partial v_r}{\partial r} + v_z \frac{\partial v_r}{\partial z} = \nu \left[\frac{1}{r} \frac{\partial}{\partial r} \left(r \frac{\partial v_r}{\partial r} \right) - \frac{v_r}{r^2} \right] \tag{27}$$

transformed to the following integral form

$$\frac{d}{dz} \int_b^a rv_r v_z dr = \nu \left[r \frac{\partial v_r}{\partial r} \Big|_{r=a} - r \frac{\partial v_r}{\partial r} \Big|_{r=b} - \int_b^a \frac{v_r}{r} dr \right] \tag{28}$$

To solve the main problem, Eqs. (22) and (26), assume the longitudinal velocity profile in the following form

$$v_z = B[2(a-b)(a-r) - (a-r)^2] \tag{29}$$

which satisfies the no-slip condition $v_z = 0$ at $r = a$ at the nozzle wall, and the no-traction condition $\partial v_z / \partial r|_{r=b} \approx 0$ at the film surface; $B = B(z)$ is the function to be found.

Note that for the supplementary problem (28), accounting for the kinematic condition (17), one should take accordingly,

$$v_r = B(a-b)(a-r) \frac{db}{dz} + D[(a-r)^2 - (a-b)(a-r)] \tag{30}$$

where $D = D(z)$ is another function to be found.

Substituting Eq. (29) into Eq. (22) and evaluating the integral, one finds

$$B = \frac{Q}{2\pi} \frac{1}{[a^4/4 - a^2b^2/2 - a^3b/3 + ab^3 - 5b^4/12]} \tag{31}$$

Similarly, substituting Eqs. (29) and (16) into Eq. (26) and evaluating the integral, one obtains

$$\begin{aligned} & \frac{d}{dz} \left\{ B^2 \left[\frac{a^6}{6} + 2a^3b^3 - \frac{17}{6}a^2b^4 + \frac{5}{3}ab^5 - \frac{a^4b^2}{6} - \frac{7}{15}a^5b - \frac{11}{30}b^6 \right] \right\} \\ &= -\Omega_0^2 \left\{ \frac{db}{dz} \left[-\frac{a^2}{2b^3} + \frac{3}{2b} - \frac{3}{2} \frac{b}{a^2} + \frac{b^3}{2a^4} \right] \right. \\ & \left. + \frac{da}{dz} \left[\frac{2(a^2-b^2)}{a^3} \ln \frac{a}{b} - \frac{3}{2a} + \frac{2b^2}{a^3} - \frac{b^4}{2a^5} \right] \right\} - 2\nu a B(a-b) \end{aligned} \tag{32}$$

Substitute B from Eq. (31) into Eq. (32) and differentiate by z. Then, one arrives at the following dimensionless equation for the dimensionless film thickness \bar{b}

$$\frac{d\bar{b}}{d\bar{z}} = \frac{F_2}{F_1} \frac{d\bar{a}}{d\bar{z}} + \frac{F_3}{F_1} \tag{33}$$

where a, b, and z are rendered dimensionless using the nozzle entrance radius $a_0 = D_s/2$, and the functions F_1 , F_2 and F_3 are given by the following formulae

$$\begin{aligned} F_1 = & \frac{[6a^3\bar{b}^2 - (34/3)a^2\bar{b}^3 - (25/3)a\bar{b}^4 - a^4\bar{b}/3 - (7/15)a^5 - (11/5)\bar{b}^5]}{[a^4/4 - a^2\bar{b}^2/2 - a^3\bar{b}/3 + a\bar{b}^3 - (5/12)\bar{b}^4]^2} \\ & - \frac{2[a^6/6 + 2a^3\bar{b}^3 - (17/6)a^2\bar{b}^4 + (5/3)a\bar{b}^5 - a^4\bar{b}^2/6 - (7/15)a^5\bar{b} - (11/30)\bar{b}^6]}{[a^4/4 - a^2\bar{b}^2/2 - a^3\bar{b}/3 + a\bar{b}^3 - (5/12)\bar{b}^4]^3} \\ & \times [-a^2\bar{b} - \bar{a}^3/3 + 3a\bar{b}^2 - (5/3)\bar{b}^3] \\ & + \bar{\Omega}_0^2 \left[-\frac{a^2}{2\bar{b}^3} + \frac{3}{2\bar{b}} - \frac{3}{2} \frac{\bar{b}}{a^2} + \frac{\bar{b}^3}{2a^4} \right] \end{aligned} \tag{34}$$

$$\begin{aligned} F_2 = & \frac{[a^5 + 6a^2\bar{b}^3 - (17/3)a\bar{b}^4 + (5/3)\bar{b}^5 - (2/3)a^3\bar{b}^2 - (7/3)a^4\bar{b}]}{[a^4/4 - a^2\bar{b}^2/2 - a^3\bar{b}/3 + a\bar{b}^3 - (5/12)\bar{b}^4]^2} \\ & - \frac{2[a^6/6 + 2a^3\bar{b}^3 - (17/6)a^2\bar{b}^4 + (5/3)a\bar{b}^5 - a^4\bar{b}^2/6 - (7/15)a^5\bar{b} - (11/30)\bar{b}^6]}{[a^4/4 - a^2\bar{b}^2/2 - a^3\bar{b}/3 + a\bar{b}^3 - (5/12)\bar{b}^4]^3} \\ & \times [\bar{a}^3 - a\bar{b}^2 - \bar{a}^2\bar{b} + \bar{b}^3] \\ & - \bar{\Omega}_0^2 \left[\frac{2(\bar{a}^2 - \bar{b}^2)}{\bar{a}^3} \ln \frac{\bar{a}}{\bar{b}} - \frac{3}{2\bar{a}} + \frac{2}{3} \frac{\bar{b}^2}{\bar{a}^3} - \frac{\bar{b}^4}{2\bar{a}^5} \right] \end{aligned} \tag{35}$$

$$F_3 = -\frac{1}{\text{Re}} \frac{(\bar{a}^2 - a\bar{b})}{[a^4/4 - a^2\bar{b}^2/2 - a^3\bar{b}/3 + a\bar{b}^3 - (5/12)\bar{b}^4]} \tag{36}$$

In Eqs. (34)–(36) the following dimensionless groups are involved

$$\bar{\Omega}_0^2 = \frac{4\pi^2 \Omega_0^2 a_0^2}{Q^2}, \quad \text{Re} = \frac{Q}{4\pi a_0 \nu} \tag{37}$$

which express the dimensionless swirl [known via Eq. (13)] and the Reynolds number, also known, because Q is given.

The ordinary differential Eq. (33) with the functions (34)–(36) is solved numerically using the Kutta-Merson method with the following boundary condition at the nozzle entrance

$$\bar{z} = 0: \quad \bar{b} = \bar{b}_0 \tag{38}$$

where $\bar{b}_0 = b_0/a_0$ is given.

Note also, that the nozzle profile involved on the right-hand side of Eq. (33) corresponding to that of Fig. 1 is given by the following expressions

$$\begin{aligned} \bar{a}(\bar{z}) = & 1, \quad 0 \leq \bar{z} \leq \bar{L}_s \\ \bar{a}(\bar{z}) = & \frac{D_0}{D_s} + (\bar{\varrho} - \bar{z}) \tan \alpha_c, \quad \bar{L}_s \leq \bar{z} \leq \bar{\varrho} \\ \bar{a}(\bar{z}) = & \frac{D_0}{D_s}, \quad \bar{\varrho} \leq \bar{z} \leq \bar{L} \end{aligned} \tag{39}$$

where

$$\begin{aligned} \bar{L}_s = & \frac{L_s}{D_s/2} \\ \bar{\varrho} = & \frac{L_s + [(D_s - D_0)/2] \cot \alpha_c}{D_s/2} \\ \bar{L} = & \frac{L_s + L_0 + [(D_s - D_0)/2] \cot \alpha_c}{D_s/2} \end{aligned} \tag{40}$$

3.5. Spread cone angle of the free film at the nozzle exit

The spread cone angle of the free film at the nozzle exit is governed by the centrifugal force. Namely, the second law of Newton for a material element in the swirling film reads

$$m \frac{d^2 R}{dt^2} = m \frac{v_\theta^2}{R} \Big|_{r=b, \text{ nozzle exit}} \tag{41}$$

where R is the radial position of a material element, m is its mass, and t is time.

The first integral of Eq. (41) yields

$$\left(\frac{dR}{dt} \right)^2 = 2v_\theta^2|_{r=b, \text{ nozzle exit}} \ln R + \text{const} \tag{42}$$

Because $v_r = dR/dt$ at the nozzle exit, and Eq. (17) shows that it is expected that $v_r|_{\text{nozzle exit}} \approx 0$ at the exit after the second straight section of the nozzle, the constant of integration in Eq. (42) can be found from the condition $dR/dt = 0$ at $R = b_{\text{nozzle exit}}$. Then, Eq. (42) yields $\text{const} = -2v_\theta^2|_{r=b, \text{ nozzle exit}} \ln b_{\text{nozzle exit}}$ and thus,

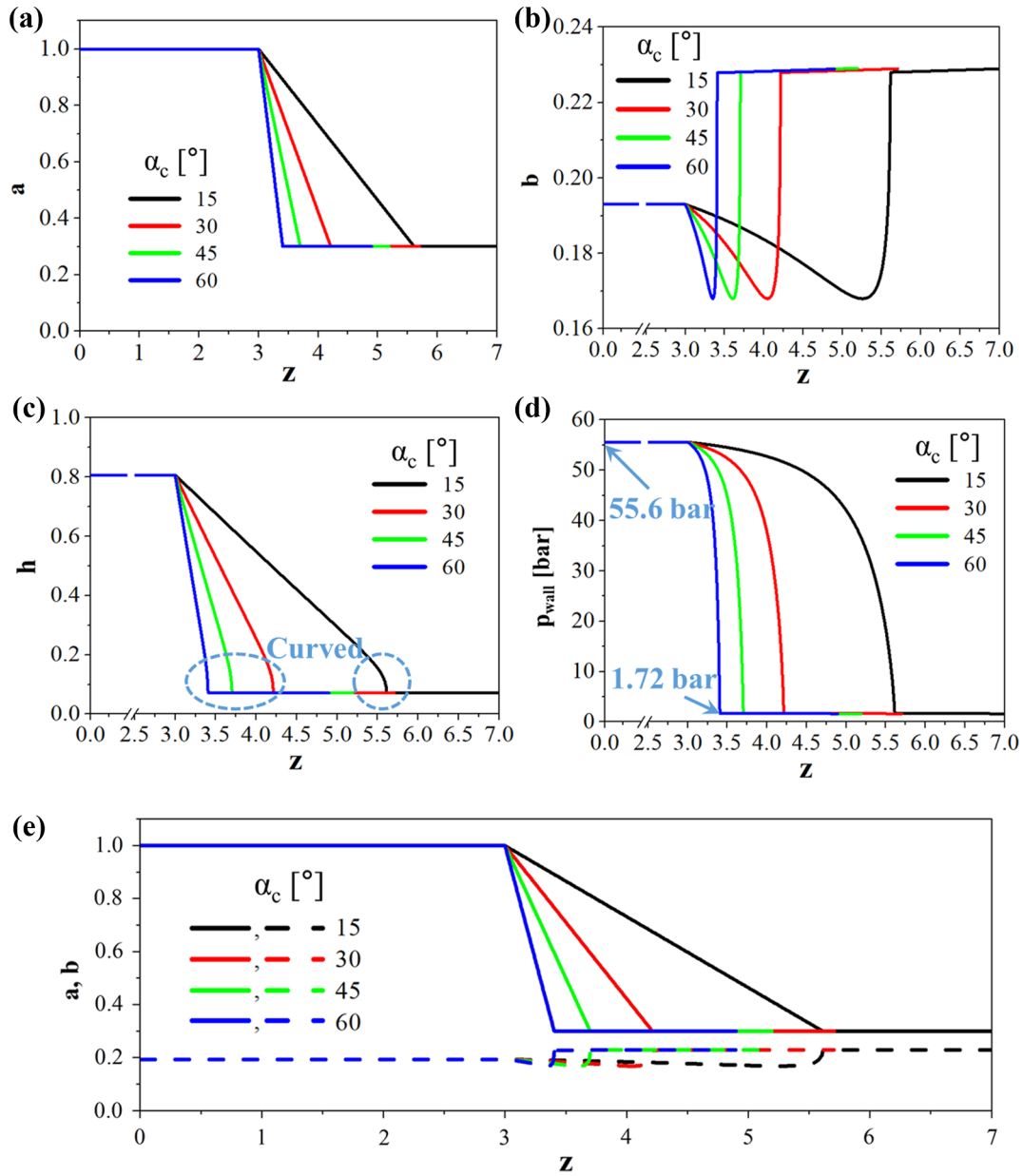


Fig. 3. Effect of nozzle convergence angle (α_c) on the dimensionless free surface radius (b), wall pressure (p), and dimensionless film thickness (h). (a) Dimensionless nozzle profile (radius), a , (b) b , (c) h , (d) p_{wall} , and (e) comparison of a and b . The nozzle convergence angle was varied from $\alpha_c = 15^\circ$ to 60° , noted as Cases 1A, 1B, 1C, and 1D in Table 1. Initial film thickness: $b_0 = 0.193$; mass flow rate: $\dot{M} = 57.3 \text{ g s}^{-1}$; orifice diameter: $D_0/D_s = 0.3$.

$$\left(\frac{dR}{dt}\right)^2 = 2v_\theta^2|_{r=b, \text{ nozzle exit}} \ln \frac{R}{b_{\text{nozzle exit}}} \quad (43)$$

Accordingly,

$$v_r|_{r=a, \text{ nozzle exit}} = \sqrt{2 \ln(a/b)_{\text{nozzle exit}}} v_\theta|_{r=b, \text{ nozzle exit}} \quad (44)$$

Then, the semi-angle of the spray cone film at the nozzle exit α is found from the expression

$$\tan \beta = \frac{v_r|_{r=a, \text{ nozzle exit}}}{v_z|_{r=b, \text{ nozzle exit}}} \quad (45)$$

Substituting Eq. (44) in Eq. (45), one obtains

$$\tan \beta = \frac{v_\theta|_{r=b, \text{ nozzle exit}}}{v_z|_{r=b, \text{ nozzle exit}}} \sqrt{2 \ln(a/b)_{\text{nozzle exit}}} \quad (46)$$

Eq. (29) yields

$$v_z|_{r=b, \text{ nozzle exit}} = B(a-b)^2|_{\text{exit}} \quad (47)$$

Also, Eq. (12) yields

$$v_\theta|_{r=b, \text{ nozzle exit}} = \frac{\Omega_0}{b} \left(1 - \frac{b^2}{a^2}\right) \Big|_{\text{exit}} \quad (48)$$

Then, using Eqs. (47), (48) and (31), one obtains

$$\frac{v_\theta|_{r=b, \text{ nozzle exit}}}{v_z|_{r=b, \text{ nozzle exit}}} = \frac{2\pi\Omega_0}{ba^2Q} \frac{(a^2 - b^2)}{(a-b)^2} [a^4/4 - a^2b^2/2 - a^3b/3 + ab^3 - 5b^4/12] \Big|_{\text{exit}} \quad (49)$$

Using Eq. (46) and (49) and rendering parameters dimensionless, one find the semi-angle in the following form

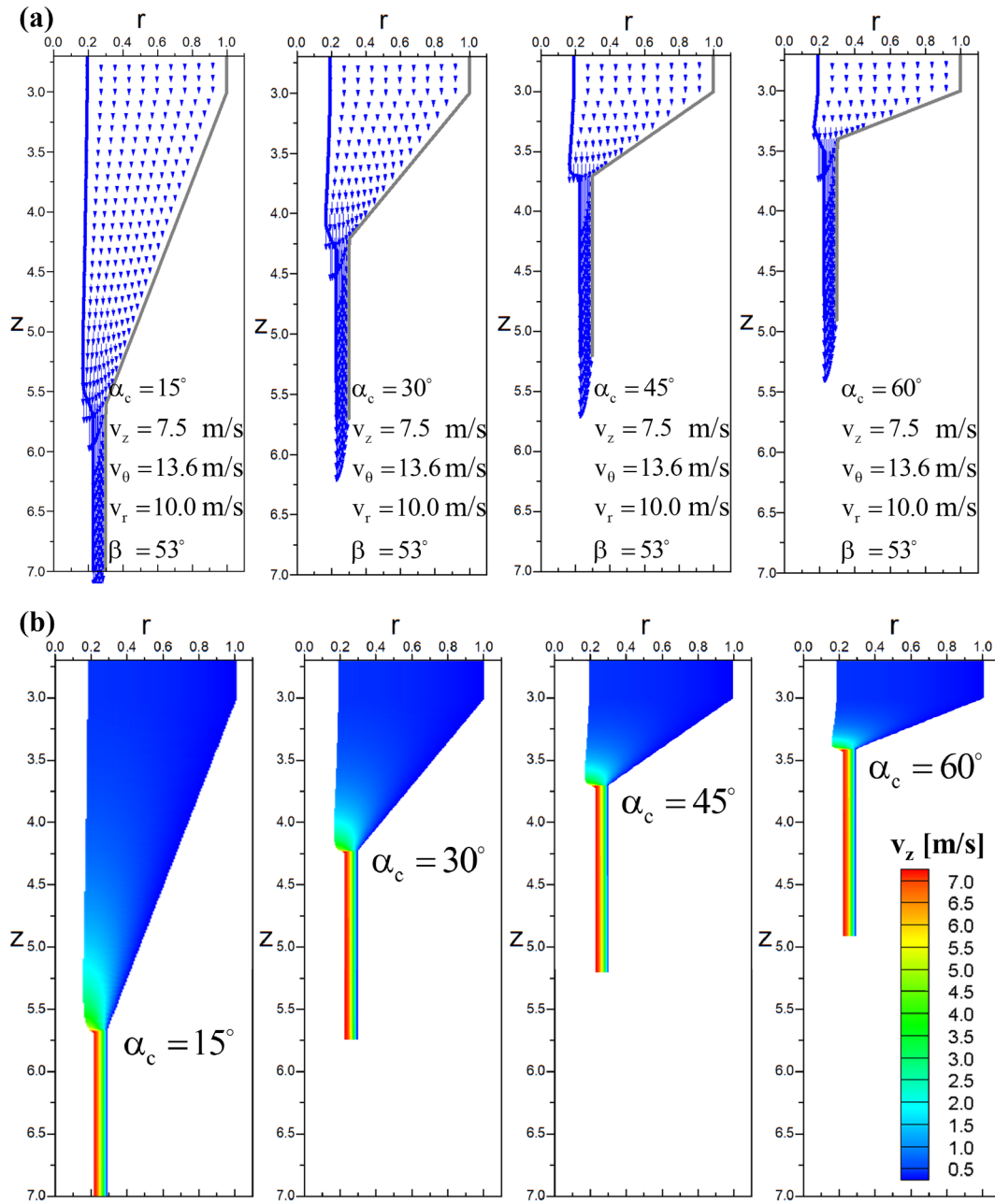


Fig. 4. Effect of α_c on the velocity field. (a) v_z vectors. (b) v_z contours. (c) v_θ contours at the upper chamber (left), the convergent part center (middle), and the nozzle exit (right). This is the benchmark Case 1C in Table 1.

$$\beta = \arctan \left\{ \bar{\Omega}_0 \frac{(\bar{a}^2 - \bar{b}^2)}{\bar{b}\bar{a}^2(\bar{a} - \bar{b})^2} [\bar{a}^4/4 - \bar{a}^2\bar{b}^2/2 - \bar{a}^3\bar{b}/3 + \bar{a}\bar{b}^3 - (5/12)\bar{b}^4] \right\}_{exit} \times \sqrt{2 \ln(\bar{a}/\bar{b})_{nozzle\ exit}} \quad (50)$$

4. Results and discussion

4.1. Effect of nozzle convergence angle

Fig. 3 shows the effect of the nozzle convergence angle (α_c) on the dimensionless free surface radius (b), wall pressure (p), and dimensionless film thickness (h). The film thickness is defined as $h = a - b$, as noted in Fig. 1c. The radii a and b are reckoned from the centerline. The nozzle convergence angle was varied from $\alpha_c = 15^\circ$ to 60° , as shown in Fig. 3a. The predicted free surface radius of the

swirling liquid film is shown in Fig. 3b. From the dimensionless coordinate $z = 3$, in all the cases the free surface radius decreased abruptly in the converging part of the nozzle, and then slightly increased again until reaching a plateau corresponding to a cylindrical free surface in the thin section of the nozzle up to the exit. This sudden fall-and-rise pattern corresponds to a slightly curved shape at the end of the converging section in Fig. 3c, where in all cases $D_0/D_s \leq 0.4$.

The wall pressure imposed by the swirling liquid was predicted according to Eq. (15) and is shown in Fig. 3d. In the upstream or upper chamber, the maximal wall pressure was $p_a = 55.6$ bar; the wall pressure gradually declined downstream as the liquid film passed through the converging nozzle section and the orifice, where the wall pressure ($r = a$) decreased to $p = p_a = 1.72$ bar in the exit part. In the upper chamber, the film was thick, and thus the mass of the film resulted in a relatively high wall pressure ($p = 55.6$ bar) associated with the centrifugal force. However, in the downstream part of the nozzle, a

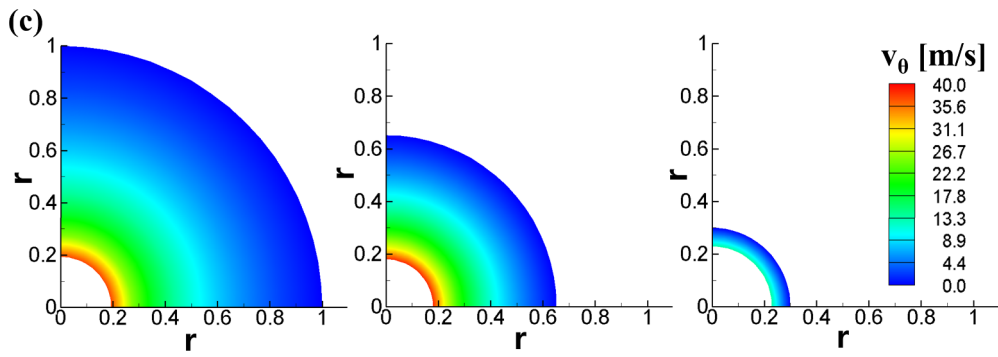


Fig. 4. (continued)

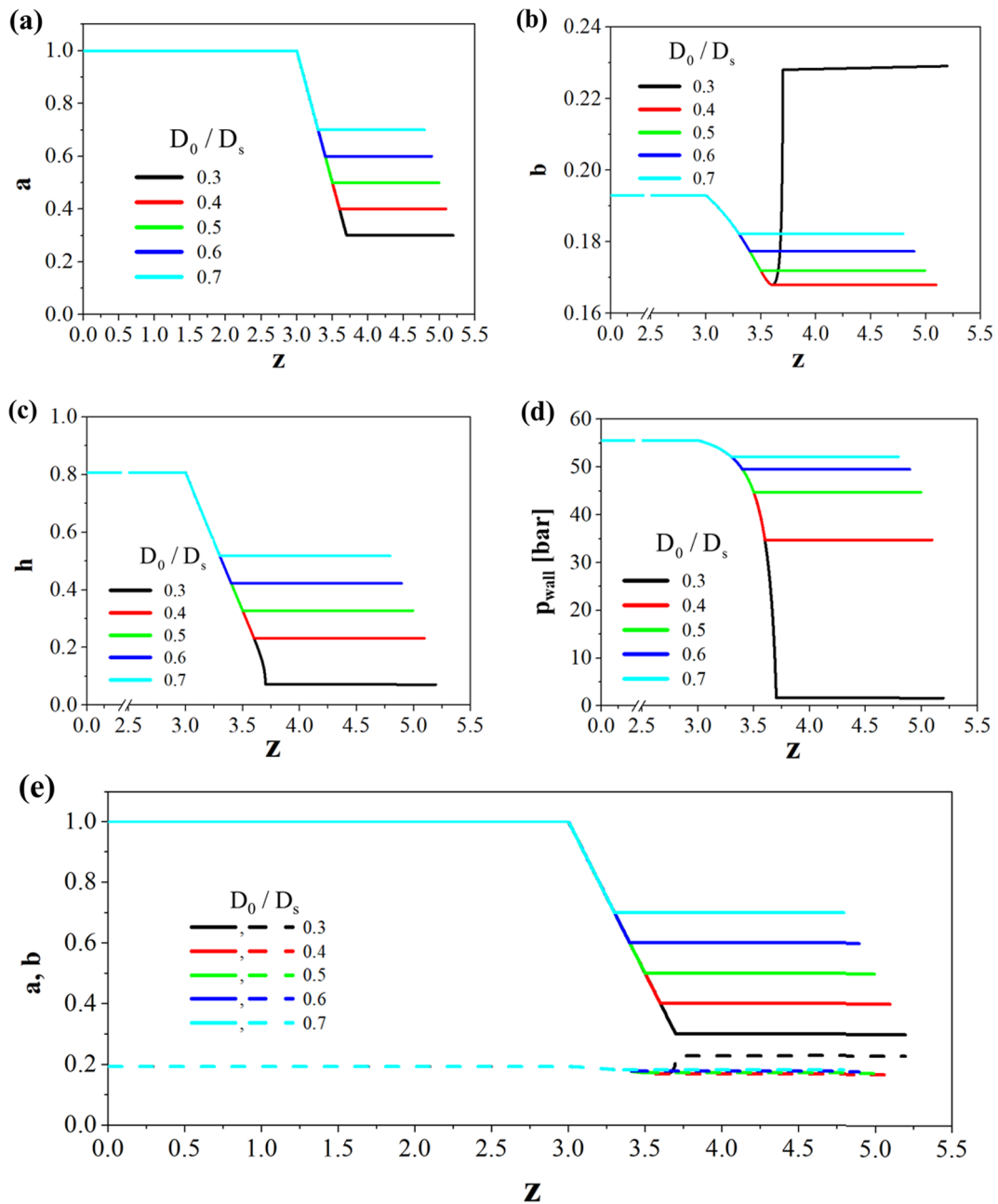


Fig. 5. Effect of nozzle convergence angle (α_c) on the free surface radius (b), wall pressure (p), and film thickness (h). (a) Nozzle outer geometry, radius a , (b) radius b , (c) thickness h , (d) pressure p_{wall} , and (e) comparison of a and b . The nozzle diameter ratio was varied from $D_0/D_s = 0.3$ to 0.7 , denoted as Cases 2A, 2B, 2C, 2D, and 2E in Table 1. The nozzle convergence angle is $\alpha_c = 45^\circ$; the initial film thickness is $\bar{b}_0 = 0.193$; the mass flow rate is $\dot{M} = 57.3 \text{ g s}^{-1}$.

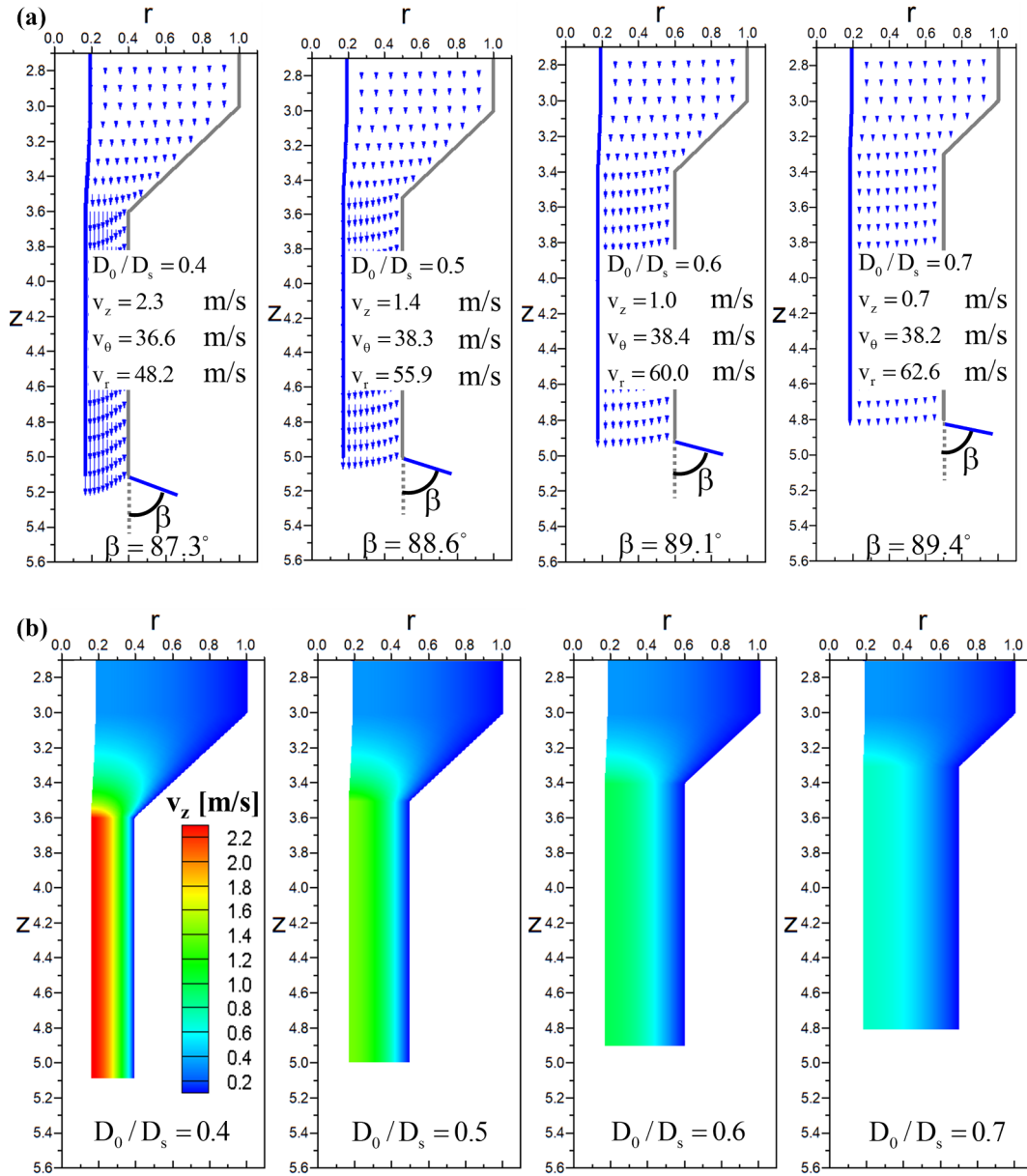


Fig. 6. Effect of D_0/D_s on the velocity field. (a) v_z vectors. (b) v_z contours. (c) v_θ contours at the upper chamber (first row), the convergent part center (second row), and the nozzle exit (third row).

very thin film of liquid that adhered to the wall resulted in a lower wall pressure of $p = 1.72$ bar. This liquid pressure at the free surface $r = b$ was always zero, which corresponds to the atmospheric gauge pressure.

The film thickness in the downstream orifice was constant and the same for all values of α_c . Therefore, the change in α_c does not affect the film thickness, except in the converging nozzle section.

Fig. 4 depicts the predicted velocity field in nozzles with different convergence angles. The dimensionless film thickness at the nozzle entrance was $\bar{b}_0 = 0.193$, and therefore, an air core was present at $0 \leq r \leq 0.193$. Except in the convergent section, the radial component is very small in the upper chamber and downstream cylindrical channel. Even though the radial velocity component v_r is nearly zero within the entire nozzle, v_r becomes non-zero as soon as the film exits the nozzle at the nozzle wall, $r = a$; cf. Eq. (44). The axial velocity component v_z was computed using Eqs. (29) and (47) at the free surface, $r = b$, where v_z is maximum. The spray-cone angle at the nozzle exit is found using Eq. (45), which accounts for the ratio of v_r at $r = a$ and v_z at $r = b$. It was found that the spray-cone angle (β) did not change with the variation of α_c , as indicated in the vector plots in

Fig. 4a. Note that tangential velocity at the nozzle exit is $v_\theta = 13.6$ m/s at the free surface ($r = b$).

In Fig. 4b, the velocity components v_z were maximal at the free surface ($r = b$) and zero because of the no-slip boundary condition at the nozzle wall ($r = a$). The flow accelerates toward the nozzle exit because of the continuity equation. Indeed, from the upper chamber to the downstream orifice, the liquid film thickness decreases drastically and thus the axial velocity component must increase to sustain the constant mass flow rate along the nozzle. The contour plots in Fig. 4b depict the magnitude of v_z , wherein, the free surface of the film is clearly visible.

The tangential component of the velocity (v_θ) is described by Eq. (12), which implies that v_θ is maximal at the free surface ($r = b$), and approaches zero at the wall ($r = a$), where the no-slip condition holds, as in Fig. 4c. This trend of v_θ was consistent throughout the nozzle (from $z = 0$ to $z = \text{exit}$). Fig. 4c also presents the distributions of v_θ in the cross-sectional areas of the upper chamber (left), the middle of the convergent section (middle), and the nozzle exit (right). The magnitude of the tangential velocity can reach up to $v_\theta \sim 37$ m/s at $r = b$ in the

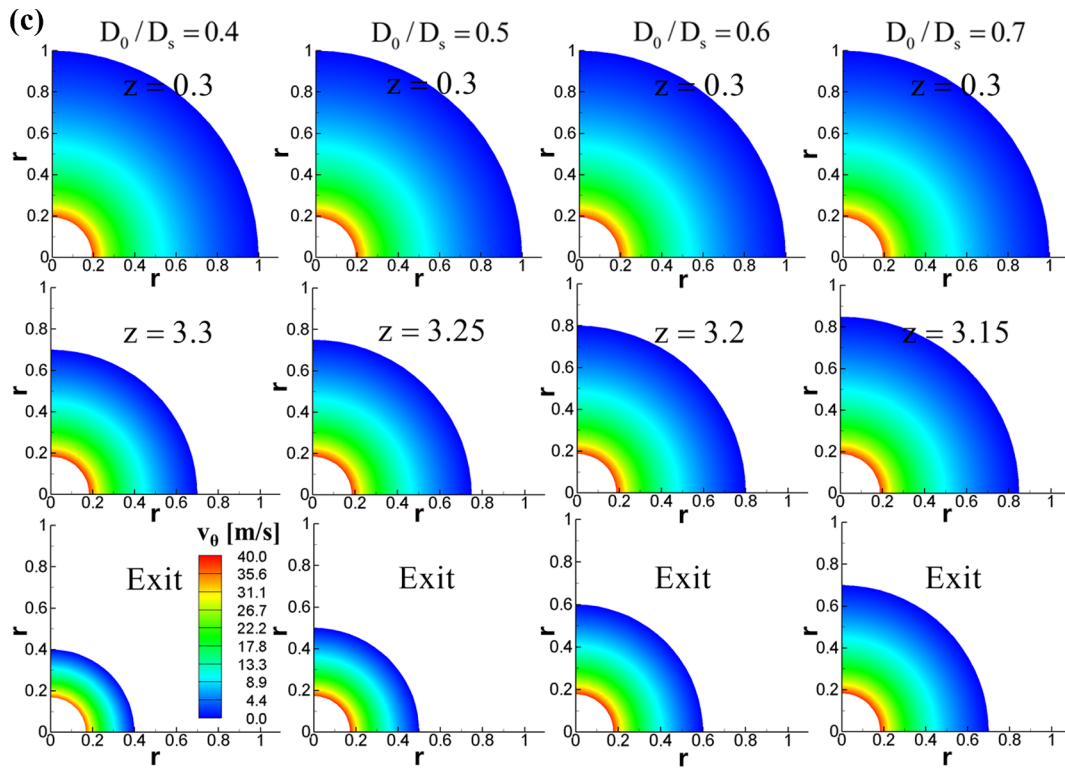


Fig. 6. (continued)

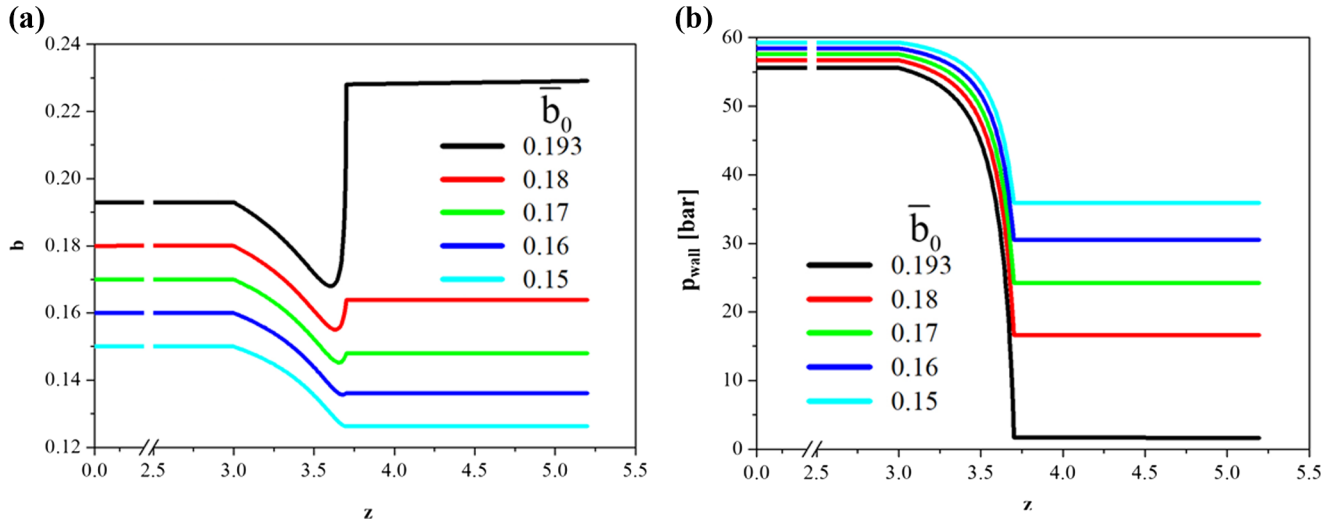


Fig. 7. Effect of the initial film thickness, \bar{b}_0 , on (a) the free surface radius b , and (b) wall pressure, p_{wall} . The initial film thickness was varied from $\bar{b}_0 = 0.193$ to 0.15, denoted as Cases 3A, 3B, 3C, 3D, and 3E in Table 1. The nozzle convergence angle is $\alpha_c = 45^\circ$; the orifice diameter ratio is $D_0/D_s = 0.3$; the mass flow rate is $\dot{M} = 57.3 \text{ g s}^{-1}$.

upper chamber; however, v_θ reduces to 13.6 m/s at the nozzle exit. It should be noted that Eq. (12) describes v_θ as a function of the radial position r (including the free surface location $r = b$) and the wall boundary (a). Even though the free surface location might be identical, the tangential velocity at the free surface might be different if the wall boundary location (a) is different. For example, the value of a is greater in the upper chamber than in the orifice section and, thus, v_θ at the free surface would be larger in the upper chamber according to Eq. (12). As a result, the free surface tangential velocity is $v_\theta \sim 37 \text{ m/s}$ in the upper chamber where the dimensionless $a = 1$ and $v_\theta \sim 13.6 \text{ m/s}$ in the orifice section where $a = 0.3$ (i.e., $D_0/D_s = 0.3$).

4.2. Effect of nozzle exit diameter

Fig. 5 depicts how the change in the nozzle diameter ratio (D_0/D_s) affects the location of the free surface, film thickness and pressure distribution, with D_0 and D_s being the orifice and swirling chamber diameters, respectively, as depicted in Fig. 1c. The reduction in the orifice diameter is shown in Fig. 5a. The free surface location and the film thickness changed with the variation of D_0/D_s . In particular, in Fig. 5c the results demonstrate that the film thickness increased as the ratio D_0/D_s decreased. The wall pressure in the upper chamber was constant for all cases (Fig. 5d), but decreased upon entering the downstream part of the nozzle. When $D_0/D_s = 0.7$, i.e. the nozzle convergence was small, the film at the nozzle exit was still quite thick,

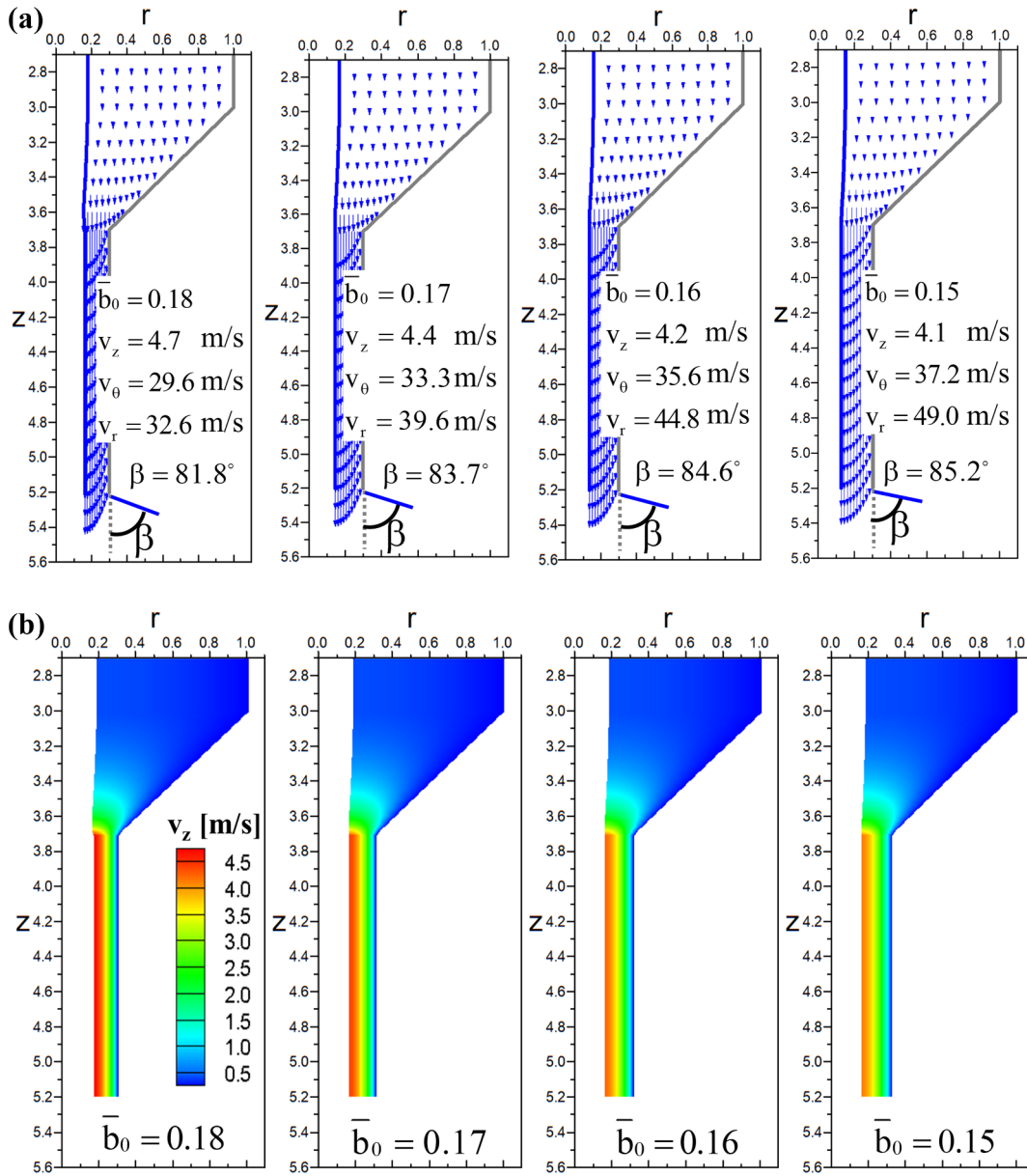


Fig. 8. Effect of \bar{b}_0 on velocity field. (a) v_z vectors. (b) v_z contours. (c) v_θ contours at the upper chamber (first row), the convergent part center (second row), and the nozzle exit (third row).

which created strong centrifugal pressure against the wall, and thus the pressure decrease was quite moderate. However, for an abrupt nozzle convergence at $D_0/D_s = 0.3$, the film thickness was greatly reduced in transition from the upper chamber to the exit part of the nozzle, and thus the pressure change was much more significant. In the exit part of the nozzle, the film is thin and does not create strong pressure against the wall because the centrifugal force is diminished with the liquid mass.

Fig. 5e compares the radii a and b . The radius of the free surface b in the converging section shown in Fig. 5b is not dramatically changing for $0.4 \leq D_0/D_s \leq 0.7$, and is, in fact, indiscernable in Fig. 5e. Only for $D_0/D_s = 0.3$, the decrease and an abrupt increase in b seen in Fig. 5b is also clearly revealed in Fig. 5e. This sudden increase in the free surface boundary radius suggests a corresponding reduction in the film thickness as a result of the narrowing of the exit diameter of the nozzle.

Narrowing of the orifice diameter of the exit section from $D_0/D_s = 0.7$ to 0.4 , naturally increases flow velocity, as shown in Fig. 6a. The axial length of the convergent section varies slightly while connecting the varying diameter of the orifice section with the upper

chamber. With reducing D_0/D_s , the axial velocity increases from $v_z = 0.7$ to 2.3 m/s, while the radial velocity decreases from $v_r = 62.6$ to 48.2 m/s. As a result, the cone-angle slightly decreases from $\beta = 89.4$ to 87.3° . The vector plots in Fig. 6a indicate that all velocity profiles were parabolic in shape, yielding the maximum velocity at the free surface ($r = b$) and zero velocity at the wall ($r = a$). The axial velocity increased with narrowing of the orifice diameter. As mentioned earlier, the radial component of the velocity was nearly zero within the nozzle; $v = \sqrt{v_z^2 + v_r^2} \sim v_z$. However, the centrifugal force enforces the swirling film to generate radial velocity in the absence of the wall at the nozzle exit. This radial velocity was maximal ($v_r = 62.6$ m/s) at the highest value of $D_0/D_s = 0.7$, yielding the largest cone angle of $\alpha = 89.4^\circ$ at the nozzle exit. In contrast, when D_0/D_s was reduced to 0.4 , the axial velocity increased ($v_z = 2.3$ m/s) owing to acceleration of the flow in response to the reduced orifice diameter. Therefore, the cone angle decreased slightly to $\alpha_c = 87.3^\circ$.

In Fig. 6b, the magnitude of v_z is shown for the various values of D_0/D_s . The v_z magnitude increases as reducing D_0/D_s at the constant mass flow rate. Fig. 6c shows the contour levels of the tangential velocity (v_θ)

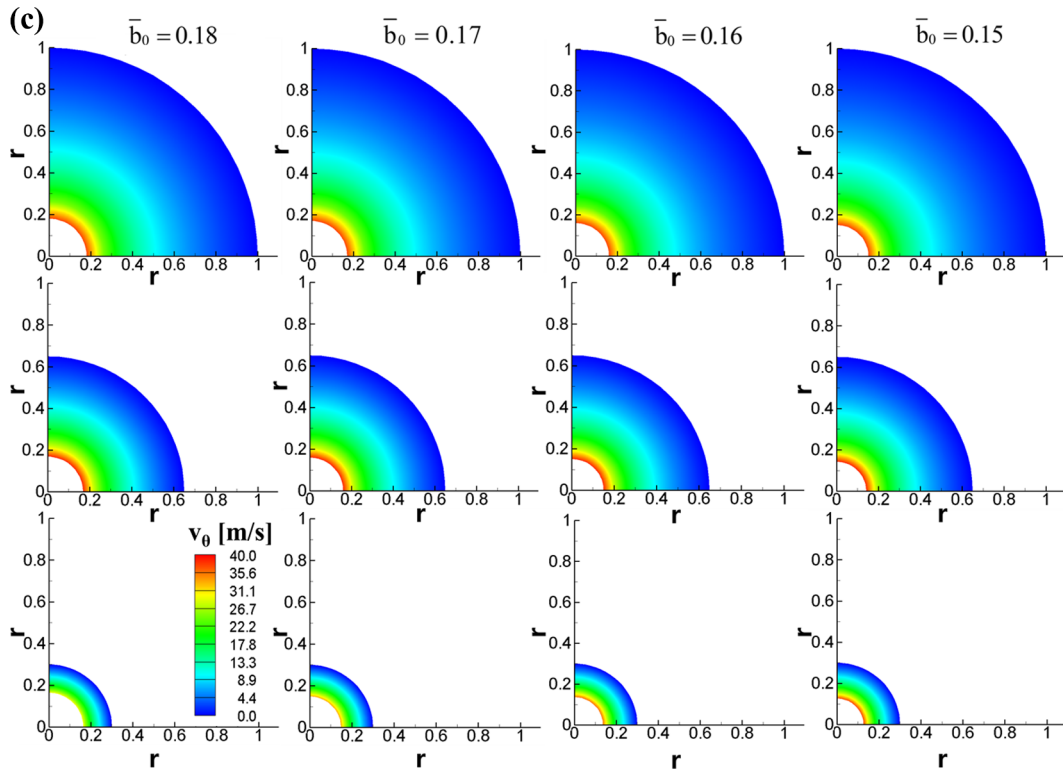


Fig. 8. (continued)

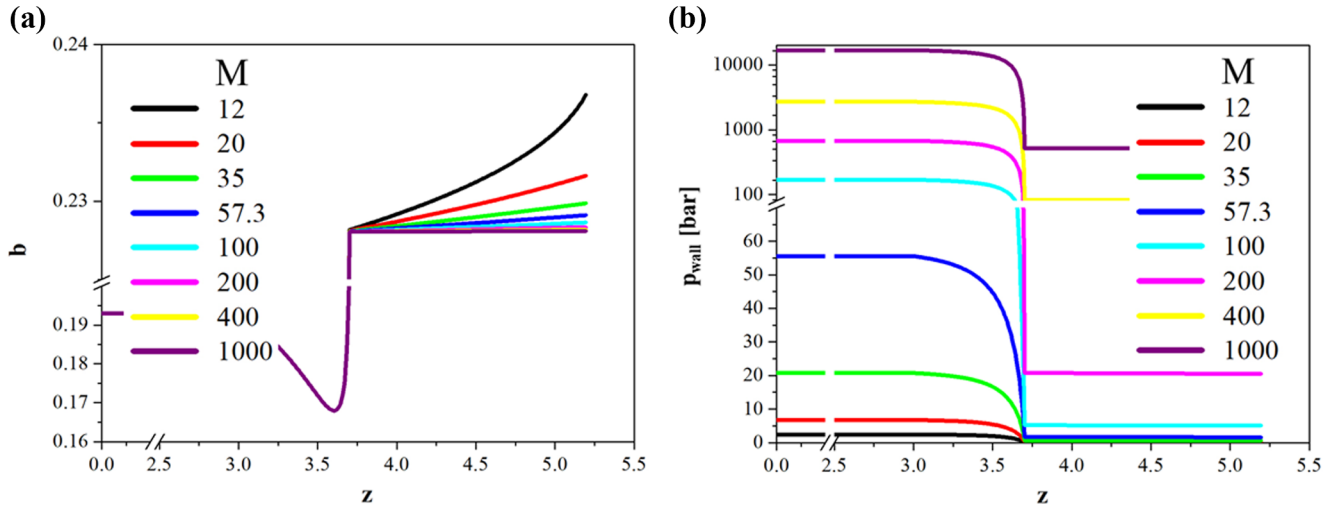


Fig. 9. Effect of the mass flow rate, \dot{M} , on (a) the free surface radius b , and (b) wall pressure, p_{wall} . The mass flow rate was varied from $\dot{M} = 12$ to $1000 \text{ g}\cdot\text{s}^{-1}$, denoted as Cases 4A–4H in Table 1. The nozzle convergence angle is $\alpha_c = 45^\circ$; the orifice diameter ratio is $D_0/D_s = 0.3$; the initial film thickness is $\bar{b}_0 = 0.193$.

in the upper chamber ($z = 0.3$), the middle convergent section ($3.15 \leq z \leq 3.3$), and at the orifice exit ($z = z_{\text{max}}$) for the various values of D_0/D_s . In the upper chamber ($z = 0.3$), there is no difference in the v_θ distribution. At the orifice exit ($z = z_{\text{max}}$), the tangential velocity slightly decreased from $v_\theta = 38.2$ to 36.6 m/s when D_0/D_s is reduced from 0.7 to 0.4, as already indicated in Fig. 6a. When D_0/D_s was further reduced to $D_0/D_s = 0.3$ (i.e., in Case 1C), the tangential velocity was substantially reduced to $v_\theta = 13.6 \text{ m/s}$. It should be noted that Eq. (12) describes the variation of v_θ as a function of the radial location (r) and the wall boundary (a), which varies in concert with the value of the ratio D_0/D_s .

4.3. Effect of the initial film thickness

Fig. 7 presents the effect of the initial film thickness \bar{b}_0 on the free

surface radius b and the wall pressure p_{wall} . A larger value of \bar{b}_0 suggests a thinner film as the free surface approaches the wall with fixed nozzle geometry. When the mass flow rate is fixed and the film is thinned, a faster moving film is produced within the nozzle. In contrast, a thicker film with smaller \bar{b}_0 would produce a higher pressure because of the larger liquid mass driven in swirling motion. Therefore, the wall pressure is higher when \bar{b}_0 is smaller, as observed in Fig. 7b.

Fig. 8 shows the effect of \bar{b}_0 on the velocity profile. As the film thickens (or \bar{b}_0 diminishes), the axial velocity v_z diminishes to sustain the constant mass flowrate. The free surface ($r = b$) axial velocity at the orifice exit plane is shown in Fig. 8a; v_z reduces from 4.7 to 4.1 m/s. Given that the tangential velocity (v_θ) is maximum at the free surface ($r = b$) according to Eq. (12), a thinner film (which is equivalent to larger \bar{b}_0) would result in smaller v_θ at the free surface. In Fig. 8a, the tangential velocity reduces from $v_\theta = 37.2$ to 29.6 m/s as \bar{b}_0 changes

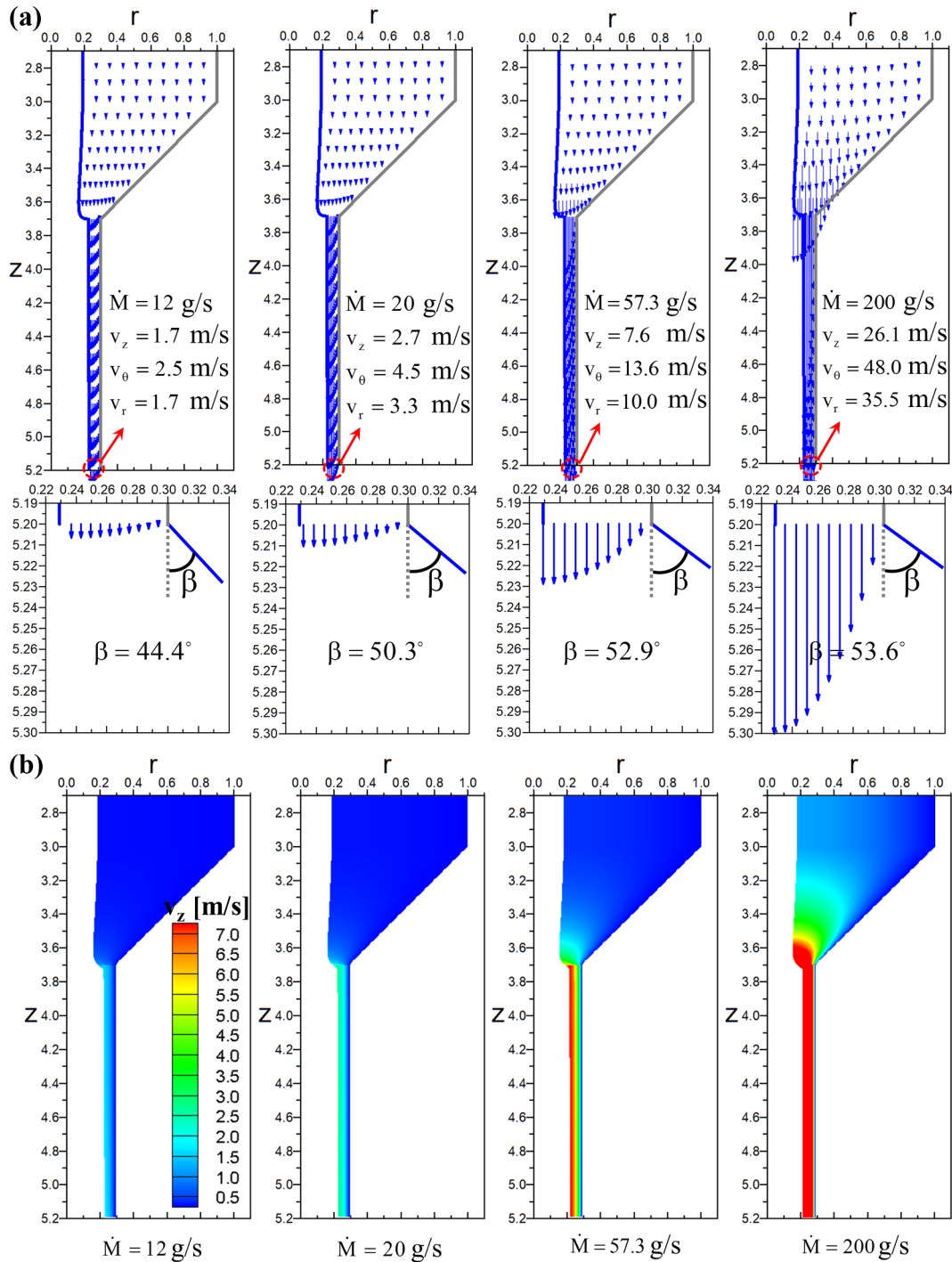


Fig. 10. Effect of \dot{M} on the velocity field. (a) v_z vectors. (b) v_z contours. (c) v_θ contours at the upper chamber (first row), the convergent part center (second row), and the nozzle exit (third row).

from 0.15 to 0.18 (i.e., the film is thinning). Accordingly, the radial velocity at the exit plane at $r = a$ also reduces from $v_r = 49$ to 32.6 m/s, while \bar{b}_0 changes from 0.15 to 0.18 because Eq. (44) indicates that v_r at $r = a$ is proportional to v_θ at $r = b$. If v_θ reduces, v_r also reduces. Overall, for a thinner film (larger \bar{b}_0), v_z increases and v_r decreases at the exit plane. As a result, the cone angle (β) decreases. Fig. 8b shows that the axial velocity increases in the orifice section when increasing \bar{b}_0 (or for a thinning film). Fig. 8c shows that the tangential velocity is reduced at larger \bar{b}_0 because a film gets thinner and the corresponding free surface ($r = b$) is located closer to the wall, where the no-slip boundary condition is imposed.

4.4. Effect of mass flow rate

Fig. 9 shows the effect of the mass flow rate, \dot{M} , on the free surface radius and wall pressure distribution, with all other parameters set constant ($\alpha_c = 45^\circ$, $D_0/D_s = 0.3$, and $\bar{b}_0 = 0.193$). As \dot{M} increased, the free surface radius, b , decreased, implying that the film thickness increased. In the exit part of the nozzle, the profile of b in the orifice deviated from uniform as \dot{M} decreased. When the mass flow rate was reduced to $\dot{M} = 12$ g/s, the free surface profile appeared to be curved, albeit insignificantly. The wall pressure, p_{wall} , is plotted in Fig. 9b for the entire range of $12 \leq \dot{M} \leq 1000$ g/s. Although the mass flow rate of $\dot{M} = 1000$ g/s is, in fact, unrealistic for the given nozzle

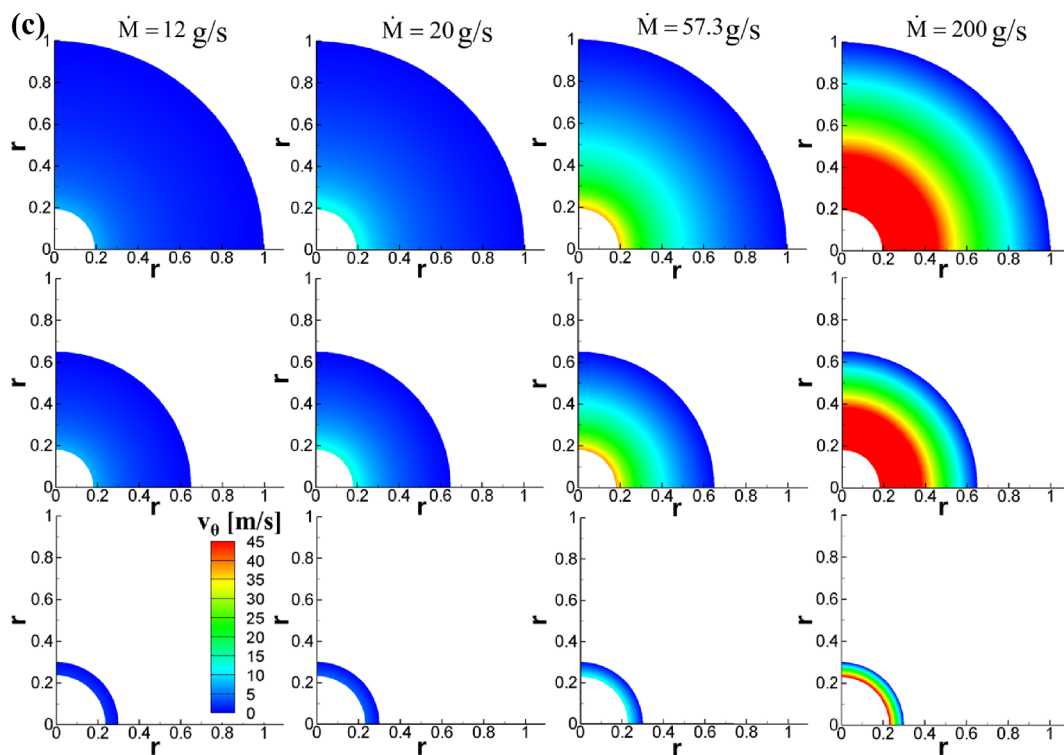


Fig. 10. (continued)

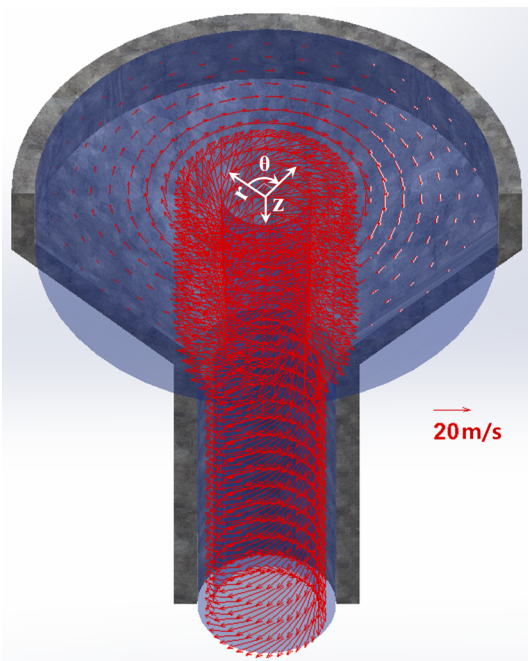


Fig. 11. Three-dimensional view of the velocity vectors of the benchmark case, Case 1C.

geometry, this hypothetical scenario is introduced to examine the corresponding wall pressure, which could be of the order of $\sim 10^4$ bar. The higher mass flow results in the higher wall pressure. In all of the cases considered herein, the wall pressure is substantially reduced as soon as the liquid enters the orifice, owing to the much thinner liquid pushing against the wall than the liquid in the upper chamber. Recall that the mass flow rate of $\dot{M} = 57.3 \text{ g s}^{-1}$ is the benchmark case introduced in Section 3.2. This produced a wall pressure of $p_{\text{wall}} \approx 55.6$ bar, as indicated in Fig. 9b.

Fig. 10 shows the velocity fields for the mass flow rate of $12 \leq \dot{M} \leq 200 \text{ g s}^{-1}$. With increasing \dot{M} , all velocity components at the exit (v_z and v_θ at $r = b$ and v_r at $r = a$) increased and the cone-angle (β) of the liquid film at the nozzle exit correspondingly increased. The free surface at the orifice entrance was severely bent, almost as a jump, in which liquid suddenly accelerated from a low to a high velocity in the axial direction. The slight bending in the free surface with decreasing \dot{M} observed in Fig. 9a is indiscernible in the vector or contour free surfaces shown in Fig. 10. This ostensible disparity is shown because the free surface change was of the order of 10^{-2} , which is insignificant in the length scale of Fig. 10.

The contours in Fig. 10b show that the axial velocity (v_z) distribution changes with increasing \dot{M} . This change in flow acceleration is visible in the orifice section, according with the variation in the mass flowrate. Fig. 10c shows the tangential velocity (v_θ) distributions with changing \dot{M} in the upper chamber, the middle convergent section, and the orifice exit. Clearly, v_θ is higher when \dot{M} is higher in the entire nozzle.

Fig. 11 shows the three-dimensional view of the velocity vectors in the middle convergent section and the orifice. It should be noted that the radial velocity is nearly zero within the nozzle because there is no radial motion of the swirling liquid inside the confining wall; only the downward axial and tangential motions are present in the nozzle. The magnitude of v_z and v_θ is maximum at the free surface because the location of $r = b$ is the furthest from the no-slip wall. The vectors in the orifice presented in Fig. 11 indicate v_z and v_θ only at the free surface for clear presentation.

4.5. Comparison with experiments

Fig. 12 summarizes the spray-cone angle predictions comprised of all results obtained in all previous sections including the effect of Case 1: the nozzle convergence angle, α_c , Case 2: the orifice diameter, D_0/D_s , Case 3: the initial film thickness, \bar{b}_0 , and Case 4: the mass flow rate, \dot{M} . As in Case 1, α_c had no effect on β . As in Case 2A, not so with the nozzle diameter ratio $D_0/D_s = 0.3$, in which the spray-cone angle differs dramatically from those for $D_0/D_s > 0.3$. As in Case 3, when \bar{b}_0 was

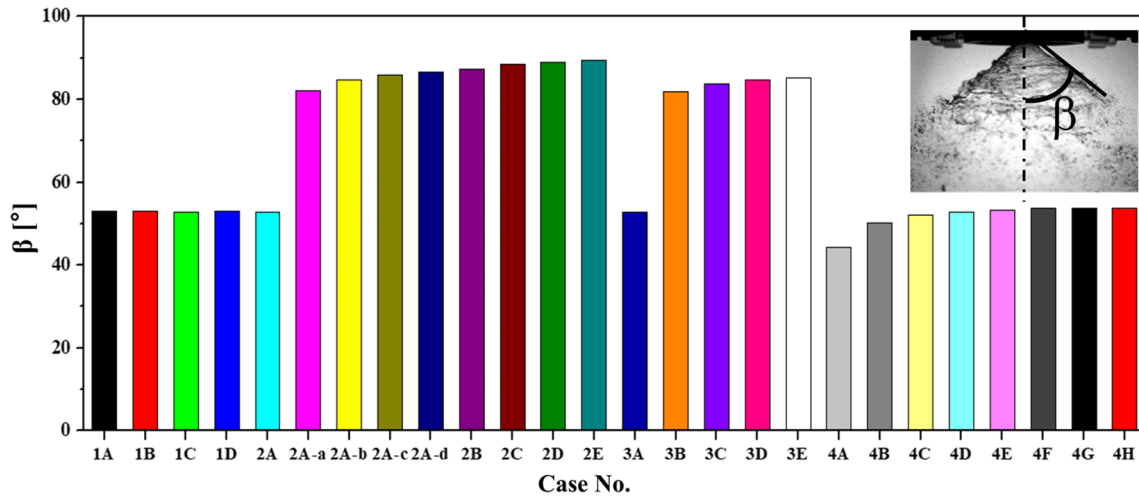


Fig. 12. Cone-angle prediction for the cases listed in Table 1.

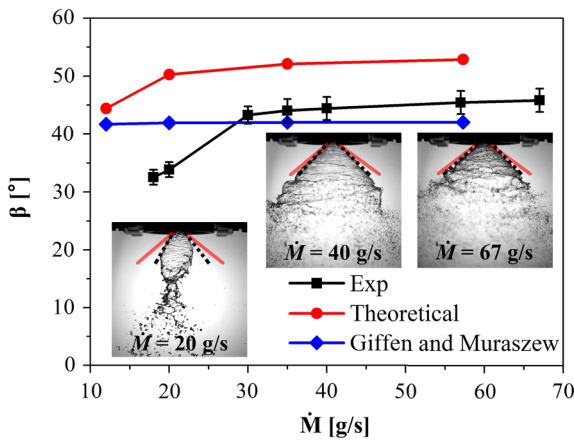
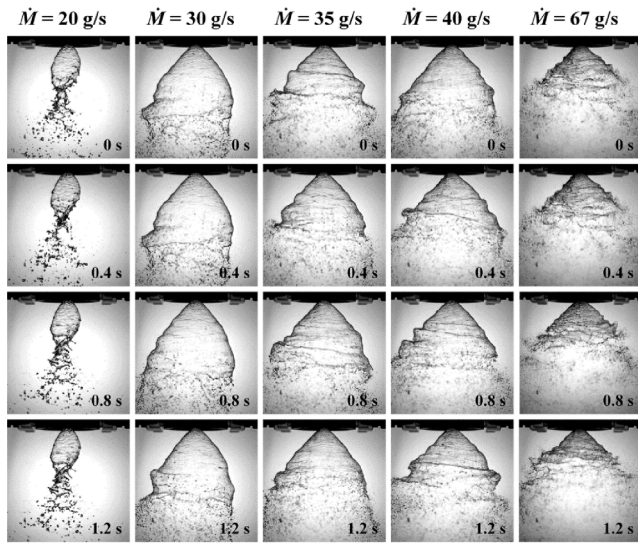


Fig. 13. (a) Time-series snapshots of the swirling liquid film revealing the spray-cone angle pattern with variation of the mass flow rate. (b) Comparison of experimental and theoretical results. The orifice diameter was fixed at $D_0/D_s = 0.3$ for both experiment and theory.

changed from 0.193 to 0.18, the spray-cone angle revealed an abrupt rise. For $b_0 \leq 0.18$ (i.e., at high film thickness), the spray-cone angle increased moderately. As in Case 4, evaluation of the effect of \dot{M} shows that the spray-cone angle changed moderately when \dot{M} was changed

from 12 to 57.3 gs^{-1} , beyond which \dot{M} essentially had no effect on β .

Fig. 13a presents the external snapshots of the swirling liquid film exiting the nozzle at the mass flow rates in the range of $20 \leq \dot{M} \leq 67 \text{ gs}^{-1}$. The swirling jets pulsed in time, especially close to the break-up end, but their shape near the nozzle exit was practically quasi-steady. Notably, the exit cone-angle did not change over time and thus the experimental cone-angle was estimated from the images of the exit cone.

There are numerous empirical formulae for predicting the spray-cone angle of the swirling liquid film [1,2,29–44]. Xue et al. [2] modified the theory of Giffen and Muraszew [15] to account for the specific nozzle geometry and orientation. Benjamin et al. [44] and Rizk and Lefebvre [29] introduced empirical formulae suitable for their operating conditions. They stated that their formulae are unsuitable for the operating conditions outside their tested range. For these reasons, the empirical formula of Giffen and Muraszew [45,46] presented below appears to be the most appropriate for comparison with the current experimental and theoretical results:

$$\tan(2\beta) = \frac{2\varepsilon}{1 + \sqrt{1 - \varepsilon}} \frac{D_s D_0}{N_t D_t^2} \quad (51)$$

where,

$$\varepsilon = \frac{(D_0/2)^2 - b^2}{(D_0/2)^2} \quad (52)$$

In Eq. (51) N_t is the number of tangential inlet ports; $N_t = 3$ in the present case. The chamber diameter in the present case was $D_s = 20 \text{ mm}$ and the exit diameter was $D_0 = 6 \text{ mm}$. The tangential port diameter was $D_t = 1.4 \text{ mm}$. While the geometric parameters of the nozzle are fixed, the radius of the air cone varies with the mass flow rate. The experimental data of the free surface locations at the exit are unavailable, only the theory could be used to estimate b . For example, when the mass flow rate increases, b decreases (or the film thickness increases). Thus, Eqs. (51) and (52) suggest that as ε increases, the spray-cone angle, β , also increases. For the mass flow rates of $\dot{M} = 12, 20, 35,$ and 57.3 gs^{-1} , the free surface radius at the nozzle exit was predicted as $b_{\text{exit}} = 2.37, 2.32, 2.30,$ and 2.29 mm , respectively. Note that $D_s/2 = r_s = 10 \text{ mm}$ was used in all the theoretical results. From Eq. (52), the corresponding ε and the spray-cone angle are $\varepsilon = 0.376, 0.404, 0.413,$ and 0.417 and $\beta = 41.68^\circ, 41.93^\circ, 42.01^\circ,$ and 42.04° , respectively. The changes in the spray-cone angle as per the Giffen and Muraszew formula appear to be quite insignificant, indicating that their empirical formula is incapable of capturing the significant spray-cone angle change when the mass flow rate is changed from low to high, as is evident from the experimental data in Fig. 13a. On the other hand, the present theoretical model is capable of capturing the significant

Table 2The free surface radius b and the spray-cone angle β predicted by the present method in comparison with previous studies.

Author	Type of data	Inlet port area, A_p [mm ²]	L_0/L_s	D_0/D_s	\dot{M} [g/s]	b/D_0	β [°]
Present work	Theoretical	10	4	0.25	50	0.67	66.83
Nouri-Borujerdi (Laminar) [12]	Numerical					0.70	68.22
Nouri-Borujerdi (Turbulent) [12]	Numerical					0.64	71.23

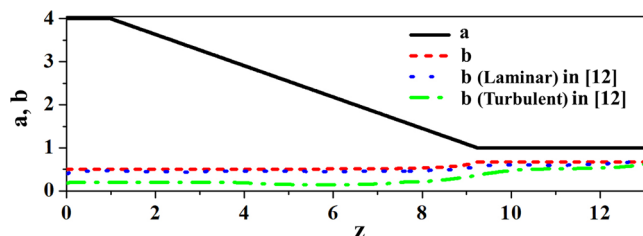


Fig. 14. The free surface radius b compared with the numerical results of Nouri-Borujerdi et al. [12]. The line denoted a depicts the nozzle profile. The red dashed line denoted b is the present prediction for the free surface radius. The blue dotted line and the green dashed-dotted line are the predictions for b from Ref. [12] (laminar and turbulent, respectively). (For interpretation of the references to colour in this figure legend, the reader is referred to the web version of this article.)

changes in the spray-cone angle with the mass flow rate, at least qualitatively, and not that far quantitatively. In addition, it is worth noting that the present method is much simpler and practical because our approach does not involve direct numerical simulation of the full Navier-Stokes equations, but rather reduces the problem to numerical integration of a single ordinary differential Eq. (33). Therefore, the current modeling effort is merited.

Fig. 13b presents the comparison of the experimental spray-cone angle with the theoretical predictions and the empirical formula of Giffen and Muraszew [45,46] in the mass flow rates of $10 \leq \dot{M} \leq 70 \text{ g s}^{-1}$. A relatively large change in the spray-cone angle was experimentally observed for the mass flow rate range of $10 \leq \dot{M} \leq 30 \text{ g s}^{-1}$, while the formula of Giffen and Muraszew predicted a nearly constant spray-cone angle in this range. The theory tended to over-predict the spray-cone for all mass flow rates. However, the character of the change in the spray-cone angle with the mass flow rate is better modelled by the current theory than by the empirical formula of Giffen and Muraszew.

In addition, the results of the numerical simulations for axisymmetric laminar and turbulent flows conducted by Nouri-Borujerdi et al. [12] have been compared with the present theoretical results in Table 2 and Fig. 14. Nouri-Borujerdi et al. [12] introduced the explicit algebraic Reynolds stress model for the laminar and turbulent Navier-Stokes equations and used the level set algorithm to model the interface between a swirling liquid film and an air core. Table 2 lists the nozzle geometric parameters, the mass flow rate, the film thickness, and the spray-cone angle at the exit. Nouri-Borujerdi et al. [12] presented two separate results; one is for laminar and the other is for turbulent flows. The turbulent flow reveals a thicker film because the turbulent eddy viscosity tends to reduce the velocity magnitude and thus, the centrifugal pressure. Fig. 14 shows that the present results are in excellent agreement with the results of direct numerical simulations of the full 3D Navier-Stokes equations by Nouri-Borujerdi et al. [12], which confirms the accuracy of the present approach.

5. Conclusion

A theoretical model of a swirling thick liquid film inside converging nozzles of various geometries was developed by solving the parabolized Navier-Stokes equations using the integral von Karman-Pohlhausen method. The governing equations were reduced to an ordinary

differential equation, with the solution being expressed in terms of the nozzle geometry and flow conditions. The thickness of the swirling liquid film inside the upper chamber and exit cylindrical part of the nozzle was predicted theoretically including the fields of the velocity components (the longitudinal and azimuthal) and pressure. The spray-cone angle of the diverging swirling liquid film at the nozzle exit was also predicted and compared with the experimental results. The main parameters governing the flow are the nozzle geometry (i.e., chamber convergence angle and the exit diameter), the initial film thickness, and mass flow rate. The mass flow rate determined the swirl strength and the corresponding Reynolds number. The major conclusions are the following ones: (i) the upper chamber convergence angle (α_c) had practically no influence on the film thickness at the nozzle exit. (ii) Decreasing the exit diameter caused both the exit film thickness and pressure to decrease, and the longitudinal velocity to increase accordingly. The spray-cone angle decreased slightly, but the change was minimal for $D_0/D_s > 0.3$. However, the cone angle changes abruptly at $D_0/D_s = 0.3$. (iii) When the initial radius of the film free surface increased (which is equivalent to a decrease in the initial film thickness), pressure decreased because of the lesser liquid mass pushing against the wall. Also, the initial radius of the film free surface increased, the longitudinal velocity component increased slightly and the spray-cone angle decreased slightly. (iv) When the mass flow rate increased, the film thickness at the exit, the spray-cone angle and the longitudinal velocity component increased.

Declaration of Competing Interest

The authors declare that they have no known competing financial interests or personal relationships that could have appeared to influence the work reported in this paper.

Acknowledgement

This work was supported by Advanced Research Center Program (NRF-2013R1A5A1073861) through the National Research Foundation of Korea (NRF) grant funded by the Korea government (MSIP) contracted through Advanced Space Propulsion Research Center at Seoul National University and NRF-2016M1A2A2936760.

References

- [1] Liu J, Zhang X-Q, Li Q-L, Wang Z-G. Effect of geometric parameters on the spray cone angle in the pressure swirl injector. *Proc Inst Mech Eng, Part G: J Aerospace Eng* 2013;227:342–53.
- [2] Xue J, Jog M, Jeng S, Steinthorsson E, Benjamin M. Effect of geometric parameters on simplex atomizer performance. *AIAA J* 2004;42:2408–15.
- [3] Li T, Nishida K, Hiroyasu H. Droplet size distribution and evaporation characteristics of fuel spray by a swirl type atomizer. *Fuel* 2011;90:2367–76.
- [4] Ma H, Wu X, Feng F, Wang D, Yang C, Zhuo C. An experimental study on fuel spray-induced vortex-like structures. *Exp Therm Fluid Sci* 2014;57:335–43.
- [5] Doumas M, Laster R. Liquid-film properties for centrifugal spray nozzles. *Chem Eng Prog* 1953;49:518–26.
- [6] Som S, Mukherjee S. Theoretical and experimental investigations on the formation of air core in a swirl spray atomizing nozzle. *Appl Sci Res* 1980;36:173–96.
- [7] Chen S, Lefebvre A, Rollbuhler J. Factors influencing the circumferential liquid distribution from pressure-swirl atomizers, (1993) 447–452.
- [8] Liao Y, Sakman A, Jeng S, Jog M, Benjamin M. A comprehensive model to predict simplex atomizer performance, ASME 1998 International Gas Turbine and Aeroengine Congress and Exhibition, American Society of Mechanical Engineers, 1998, pp. V003T006A038-V003T006A038.

- [9] Lee EJ, Oh SY, Kim HY, James SC, Yoon SS. Measuring air core characteristics of a pressure-swirl atomizer via a transparent acrylic nozzle at various Reynolds numbers. *Exp Therm Fluid Sci* 2010;34:1475–83.
- [10] Dash S, Halder M, Peric M, Som S. Formation of air core in nozzles with tangential entry. *J Fluids Eng* 2001;123:829–35.
- [11] Ibrahim AA, Jog MA. Nonlinear breakup model for a liquid sheet emanating from a pressure-swirl atomizer. *J Eng Gas Turbines Power* 2007;129:945–53.
- [12] Nouri-Borujerdi A, Kebriaee A. Numerical simulation of laminar and turbulent two-phase flow in pressure-swirl atomizers. *AIAA J* 2012;50:2091–101.
- [13] Mandal A, Jog M, Xue J, Ibrahim A. Flow of power-law fluids in simplex atomizers. *Int J Heat Fluid Flow* 2008;29:1494–503.
- [14] Taylor GI. The mechanics of swirl atomizers. *Seventh International Congress of Applied Mechanics*. 1948. p. 280–5.
- [15] Giffen E, Muraszew A. The atomization of liquid fuels. Chapman & Hall; 1953.
- [16] Abramovich G. The theory of swirl atomizer. *Ind Aerodyn* 1944:114–21.
- [17] Chinn JJ. An appraisal of swirl atomizer inviscid flow analysis, part 1: the principle of maximum flow for a swirl atomizer and its use in the exposition and comparison of early flow analyses. *Atom Sprays* 2009;19.
- [18] Taylor GI. The boundary layer in the converging nozzle of a swirl atomizer. *Q J Mech Appl Math* 1950;3:129–39.
- [19] Binnie A, Harris D. The application of boundary-layer theory to swirling liquid flow through a nozzle. *Q J Mech Appl Math* 1950;3:89–106.
- [20] Wimmer E, Brenn G. Viscous flow through the swirl chamber of a pressure-swirl atomizer. *Int J Multiph Flow* 2013;53:100–13.
- [21] Amini G. Liquid flow in a simplex swirl nozzle. *Int J Multiph Flow* 2016;79:225–35.
- [22] Dumouchel C, Bloor MIG, Dombrowski N, Ingham DB, Ledoux M. Boundary-layer characteristics of a swirl atomizer. *Atom Sprays* 1992;2:225–37.
- [23] Bang BH, Kim YI, Jeong S, Yoon Y, Yarin AL, Yoon SS. Theoretical model for swirling thin film flows inside nozzles with converging-diverging shapes. *Appl Math Model* 2019;76:607–16.
- [24] Chung Y, Kim H, Jeong S, Yoon Y. Dynamic characteristics of open-type swirl injector with varying geometry. *J Propul Power* 2016;32:583–91.
- [25] Loitsyanskii LG. *Mechanics of Liquids and Gases: International series of monographs in aeronautics and astronautics: division II: aerodynamics*. Elsevier; 2014.
- [26] Rubin SG, Tannehill JC. Parabolized/reduced Navier-Stokes computational techniques. *Annu Rev Fluid Mech* 1992;24:117–44.
- [27] Doupovec J, Yarin AL. Nonsymmetrical modified chemical vapor deposition (N-MCVD) process (optical fibres). *J Lightwave Technol* 1991;9:695–700.
- [28] Yarin AL, Nudlina TL. Thermophoretic deposition of fine particles from longitudinal flow over a cylinder. *J Aerosol Sci* 1992;23:87–95.
- [29] Rizk N, Lefebvre AH. Internal flow characteristics of simplex swirl atomizers. *J Propul Power* 1985;1:193–9.
- [30] Liu J. Experimental and numerical simulation of the breakup process of swirling conical liquid sheet. National University of Defense Technology; 2012.
- [31] Santangelo PE. Experiments and modeling of discharge characteristics in water-mist sprays generated by pressure-swirl atomizers. *J Therm Sci* 2012;21:539–48.
- [32] da Silva Couto H, Lacava PT, Bastos-Netto D, Pimenta AP. Experimental evaluation of a low pressure-swirl atomizer applied engineering design procedure. *J Propul Power* 2009;25:358–64.
- [33] Jeng S, Jog M, Benjamin M. Computational and experimental study of liquid sheet emanating from simplex fuel nozzle. *AIAA J* 1998;36:201–7.
- [34] Yinshui L, Zhuo J, Dan W, Xiaohui L. Experimental research on the water mist fire suppression performance in an enclosed space by changing the characteristics of nozzles. *Exp Therm Fluid Sci* 2014;52:174–81.
- [35] Chinn JJ. An appraisal of swirl atomizer inviscid flow analysis, part 2: inviscid spray cone angle analysis and comparison of inviscid methods with experimental results for discharge coefficient, air core radius, and spray cone angle. *Atom Sprays* 2009;19.
- [36] Moon Y, Kim D, Yoon Y. Improved spray model for viscous annular sheets in a swirl injector. *J Propul Power* 2010;26:267–79.
- [37] Fu Q-F, Yang L-J, Zhang W, Cui K-D. Spray characteristics of an open-end swirl injector. *Atom Sprays* 2012;22.
- [38] Inamura T, Tamura H, Sakamoto H. Characteristics of liquid film and spray injected from swirl coaxial injector. *J Propul Power* 2003;19:632–9.
- [39] Inamura T, Miyata K, Tamura H, Sakamoto H. Spray characteristics of swirl coaxial injector and its modeling. 37th joint propulsion conference and exhibit. 2001. p. 3570.
- [40] Ma Z. Investigation on the internal flow characteristics of pressure-swirl atomizers. University of Cincinnati; 2002.
- [41] van Banning D, Van der Geld C, Broos P, Strebe M-J. An assessment of nozzles for steam attemperation. *Exp Therm Fluid Sci* 2014;55:86–94.
- [42] Khil T, Kim S, Cho S, Yoon Y. Quantifying the variation of the mass flow rate generated in a simplex swirl injector by pressure fluctuation. 44th AIAA/ASME/SAE/ASEE joint propulsion conference & exhibit. 2008. p. 4849.
- [43] Khil T, Kim S, Cho S, Yoon Y. Quantification of the transient mass flow rate in a simplex swirl injector. *Meas Sci Technol* 2009;20:075405.
- [44] Benjamin M, Mansour A, Samant U, Jha S, Liao Y, Harris T, Jeng S. Film thickness, droplet size measurements and correlations for large pressure-swirl atomizers, ASME 1998 International Gas Turbine and Aeroengine Congress and Exhibition, American Society of Mechanical Engineers Digital Collection, 1998.
- [45] Kang Z, Wang Z-G, Li Q, Cheng P. Review on pressure swirl injector in liquid rocket engine. *Acta Astronaut* 2018;145:174–98.
- [46] Giffen E, Muraszew A. *The Atomisation of Liquid Fuels*. London: Chapman & Hall; 1953.